IPP-Report

MAX-PLANCK-INSTITUT
FÜR PLASMAPHYSIK

Raphael Gurschl

Statistical analysis of MILS experimental density measurements

IPP 2023-11
November 2023

TECHNISCHE UNIVERSITÄT WIEN

MAX-PLANCK-INSTITUT FÜR PLASMAPHYSIK

PROJEKTARBEIT

Statistical analysis of MILS experimental density measurements

ausgeführt am Max Planck Institut für Plasmaphysik
Boltzmannstraße 2
85748 Garching bei München, Deutschland

unter der Anleitung von

Dr. Maria Usoltseva

und

Dr.techn. Georg Harrer

durch

Raphael Gurschl BSc.
Matrikelnummer 11901867

Wien, October 13, 2023

Raphael Gurschl BSc.

Abstract

The energy demand of the world is constantly rising due to the growing population and emerging technologies with higher energy requirements. To meet this demand, new energy sources have to be developed and existing ones have to be improved. A reactor based on thermonuclear fusion is considered to be a very promising candidate for a solution to this problem. To create a self sustaining fusion reaction, extreme plasma conditions, not present on Earth or even in the Suns core, have to be achieved. Key plasma parameters like density and temperature need to be measured and controlled with great accuracy in a reactor. Therefore it is necessary to know the density of the plasma in the reactor.
There are different techniques to determine the density of the plasma in a reactor. The newly developed diagnostic Microwave Intensity refractometer in the Limiter Shadow (MILS) measures densities in the edge of the ASDEX Upgrade (AUG) tokamak. Through an emitter, a polarized probing wave is sent tangentially through the edge of the plasma. The wave is sent in O-mode, giving a simpler dispersion relation, depending on density only. By measuring the phase and power variation of the received signal, a radial density profile can be reconstructed.
This work focuses on the processing and analysis of the MILS data. To make the processing of the data as reliable as possible, many factors influencing the experimental data have to be taken into account. First, possible failures of the electronics components have to be excluded. It was observed, that failures originated from a high stray magnetic field in the magnetic coils closest to the MILS electronics. While hardware improvements helped to reduce the failures considerably, the identification of such events in the MILS data has to be done. Second, large signal oscillations need to be removed from the data to ensure correct density evaluation. Mostly such oscillations correspond to Edge Localized Modes (ELMs), which cause large filamentary perturbations of density in the Scrape-Off Layer (SOL). Smaller blobs/filaments are also present in the SOL in the inter-ELM periods or in the regimes where ELMs are absent, and those are filtered out as well in the MILS raw data processing, if their amplitude and duration are beyond a certain threshold. During the calibration (from Volts to Degrees and dBm), the data is checked for deviations from the calibration curves and reasons for the deviations are analyzed. The calibrated data, corrected for signal drifts induced by thermal expansion of the MILS in-vessel components, is compared to the synthetic diagnostic database and reasons for mismatches are discussed.

Contents

1 Introduction

1.1 Fusion

1.1.1 Energy sources

The continuously growing population of the Earth and the development of more energy requiring technologies demand new prospects of energy production (see Figure 1). Energy sources such as fossil fuels cannot satisfy the needs due to numerous factors. They have proven themselves to be very dangerous to our atmosphere and the climate in general. Additionally, they will run out ultimately.

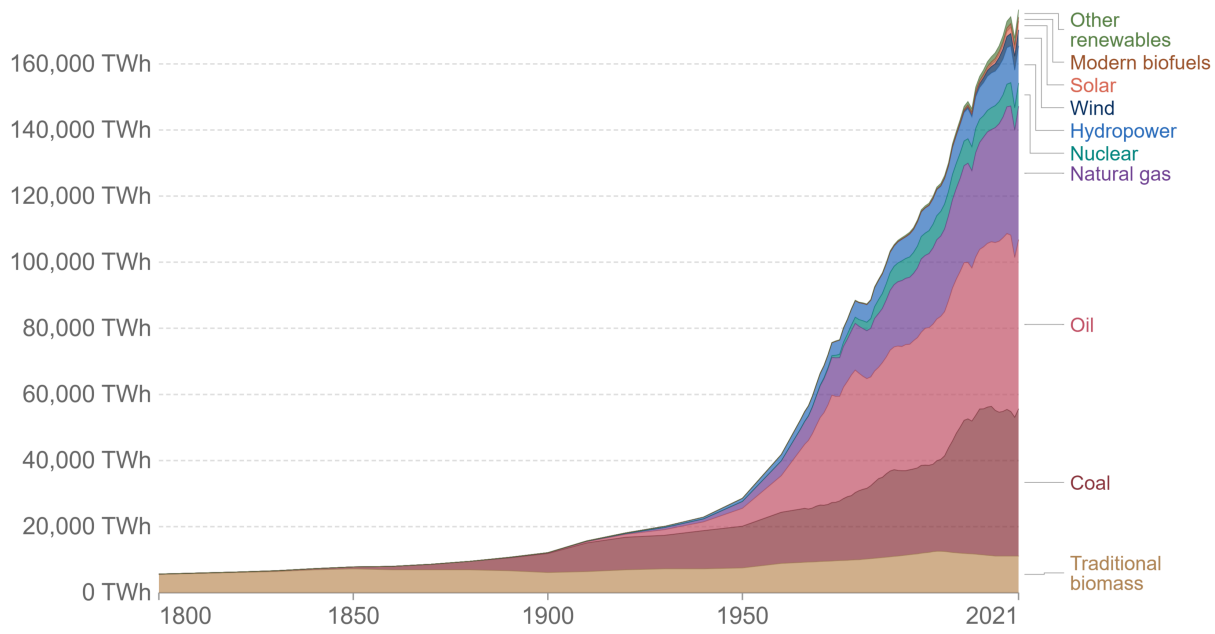

Figure 1: The worldwide energy consumption with respect to the year from 1800 to 2021. A clear trend can be seen in the increase of the energy consumption and a great amount of the energy is still produced by fossil fuels. Image adapted from [1].

Consequently, alternative solutions must be sought to replace the substantial

contribution of $\sim 130000\,\mathrm{TWh}$ from carbon-based energy sources [1]. In addition to renewable energy sources such as wind, hydropower, and solar energy, power plants utilizing nuclear fusion can also contribute to the solution. A nuclear fusion power plant would have many advantages over renewable power plants or fission power plants. First, the fuel necessary for the fusion process is abundant on earth as Tritium can be bred directly from Lithium and Deuterium can be extracted from sea water. However, a competition on Lithium use has to be taken into account. Second, it would have almost no radioactive long-time waste compared to a nuclear fission power plant. Third, due to the high energy density in a fusion reaction, only a small amount of fuel is needed compared to carbon based energy production. To produce 1000 MW electrical power, $2.7 \cdot 10^9\,\mathrm{kg}$ of coal or $1.9 \cdot 10^9\,\mathrm{kg}$ of oil would be needed. In a fusion power plant only 100 kg of Deuterium and 150 kg of Tritium could provide the same power [2]. Fourth, in contrast to renewable power plants, a fusion power plant is not dependent on weather or geographical location. These are just a few of many advantages a nuclear fusion power plant would have.

1.1.2 Thermonuclear fusion process

In thermonuclear fusion the most effective process is Deuterium Tritium fusion, due to its high reaction rate, relatively low temperature and high energy release.

$$D + T \rightarrow He + n + 17.59\,\mathrm{MeV} \tag{1.1}$$

Two nuclei, in this case Deuterium and Tritium, are combined and create another nucleus (here Helium) and other particles (e.g. neutrons). To successfully achieve this process, the Coulomb barrier must be overcome. To overcome this barrier, the atoms need high energies and collision rate to create enough reaction probability. The high energy is provided by a high enough temperature $\approx 100 \cdot 10^6$ degrees.
Consequently, one cannot talk about the thermonuclear fusion process without talking about plasma physics. Plasma is a form of matter, where the electrons and protons move independently. From the Saha Equation

$$\frac{n_\mathrm{i}}{n_\mathrm{n}} \approx 2.4 \cdot 10^{21} \frac{T^{3/2}}{n_\mathrm{i}} e^{-U_\mathrm{i}/k_\mathrm{b}T} \tag{1.2}$$

the ratio of the densities of ionized atoms n_i to neutral atoms n_n in a gas is rising with the temperature T in Kelvin [3]. Here k_b represents Boltzmann's constant and U_i the ionization energy for this gas. Therefore, with rising temperature the ionization level increases, and the plasma is fully ionized at the working temperature of a fusion power plant.
In addition to the temperature, the density of particles has to be high to ensure the necessary reaction rate according to the Lawson criterion

$$n \cdot \tau_\mathrm{E} > 5 \cdot 10^{20} \mathrm{m}^{-3}\mathrm{s} \tag{1.3}$$

at $T = 15\,\mathrm{keV}$ [4], where τ_E is the energy confinement time.

As mentioned before, not every interaction between nuclei results in a fusion process. Therefore, the hot plasma has to be confined. If not confined, the created plasma would cool down and scatter immediately. There are different possibilities to achieve confinement, among which magnetic confinement is the most advanced approach.

1.1.3 Tokamak principle and ASDEX Upgrade

One possible configuration to achieve magnetic confinement is a tokamak. The word itself comes from a Russian acronym and translates to toroidal chamber with magnetic coils. The total magnetic field necessary for the confinement consists of different magnetic fields. A toroidal magnetic field is produced by toroidal field coils around the vessel (see Figure 2). The inner poloidal field coils function as a primary winding of a transformer and the secondary winding is the plasma itself. A current in the plasma is induced which creates the poloidal magnetic field. Those two fields result in twisted, helical magnetic field lines, permitting the compensation of the vertical drift. To ensure a stable plasma configuration, an additional vertical magnetic field component is necessary [4].

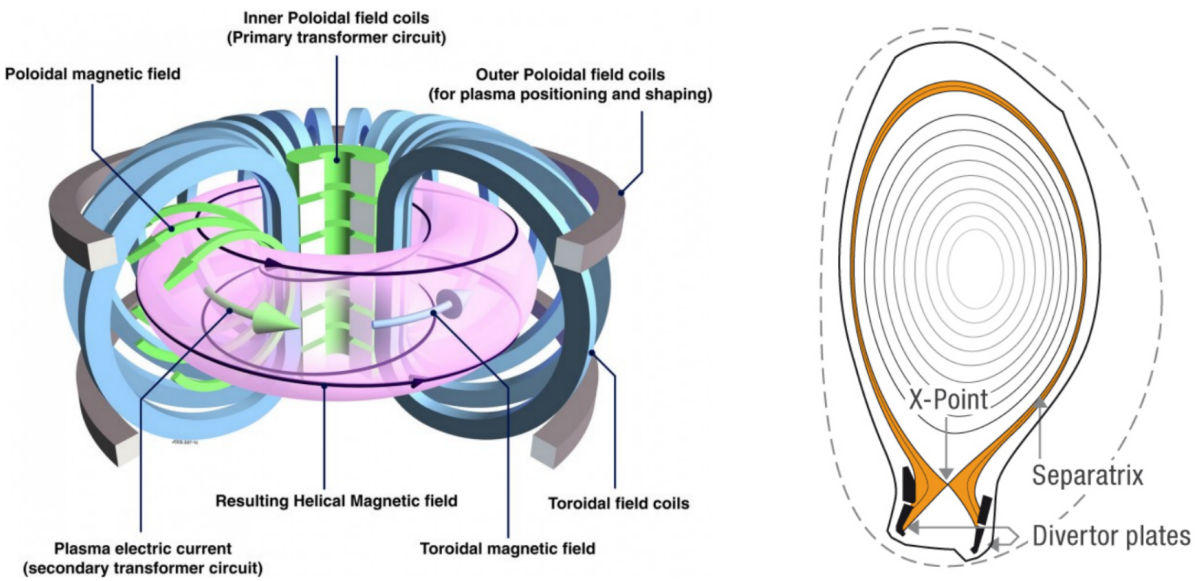

Figure 2: Left: the main structure of a tokamak is pictured. Right: a poloidal cross section of the tokamak with the magnetic field configuration and the last closed flux surface (separatrix). Figure taken from [5].

In the right part of Figure 2, a poloidal cross section of a tokamak can be seen. In gray, closed flux surfaces are shown. They are defined by $\vec{B} \cdot \vec{n} = 0$, where $\vec{B}$ is the magnetic field and $\vec{n}$ is the normal of the flux surface, meaning the magnetic flux passing through the surfaces is zero. The last closed flux surface is called separatrix and separates the region with closed magnetic field lines from the one with open ones. The flux surfaces can be determined by calculating the Magneto-Hydrodynamic (MHD) equilibrium $\vec{j} \times \vec{B} = \vec{\nabla} p$ [4], automatically yielding $\vec{B} \cdot \vec{\nabla} p = 0$. This is important because it shows that flux surfaces are surfaces of, for example, constant pressure. It is then practical to introduce a normalized radius coordinate ρ that is dependent on the flux surfaces. The radius can be defined by a parameter, that is constant along a flux surface, for example the poloidal magnetic flux, giving $\rho_{\text{poloidal}} = \sqrt{\Psi_{\text{N}}}$, where Ψ_{N} is the normalized poloidal flux. Respectively the normalized radius is one at the separatrix and zero at the plasma magnetic axis. Further plots in section 2.2 will use the normalized radius.

As the internship work used data from ASDEX (Axially Symmetric Divertor EXperiment) Upgrade (AUG), some of its characteristics are provided. The tokamak began operating in 1991 in Garching near Munich and has a major radius of 1.6 m, produces a magnetic field of up to 3.2 T and has a pulse length of up to 10 s [6]. It was designed to operate in the divertor configuration as this enables to reach the High confinement mode (H-mode) (as the one shown in Figure 2 on the right). The operating modes influence plasma parameters like the density or the confinement time significantly. For example, the energy confinement time is significantly enhanced for the H-mode in comparison to the L-mode (Low confinement time).

1.2 Density measurements in a tokamak

It is important to know the density distribution in a tokamak as it is one of the key factors for the fusion performance. This work deals with measurements of the radial density profile of the plasma edge.

There are different ways to extract information about the plasma density in the pedestal and SOL (plasma edge). In AUG, the most commonly used diagnostics for measuring edge density are Lithium/Helium-Beam Emission spectroscopy (BES) and Langmuir probes (LP) [7] [8] [9].

Li-BES/He-BES inject neutral Lithium/Helium atoms into the plasma. The atoms get excited through collisions with electrons and emit light. The line emission intensity of the excited atoms is measured. The plasma temperature and the electron density can be calculated from the measurements.

A Langmuir probe is an electrode inserted into the plasma. The voltage V of the electrode is swept and the corresponding current I is measured. The characteristic $I(V)$ curve yields information about the electron and ion density.

Additionally, in 2019 a novel diagnostic called Microwave Intensity refractometer in the Limiter Shadow (MILS) has been introduced. It will be explained in detail in section 1.3.

For the different diagnostics, measurements parameters differ considerably, in particular time resolution, accessible density range, radial span of the profile and location of the measurements. For MILS, the time resolution for the presented data is $5\,\mu$s (data acquisition is done at 10 times higher rate, but downsampling is applied in the current analysis), whereas He-BES and Li-BES are done with both 1 and 10 ms time resolution, LP with 0.5 ms. The values correspond to time interval values to achieve high enough signal to noise ratio.
MILS is able to diagnose densities ~ 5 cm around the limiter with densities from $10^{15}\,\mathrm{m}^{-3}$ to $\sim 10^{19}\,\mathrm{m}^{-3}$. He-BES measures from inside the confined region up to $1.5\,cm$ before the limiter, but densities below $10^{18}\,\mathrm{m}^{-3}$ are not measurable. The diagnostic is aimed for densities up to $4 \cdot 10^{19}\,\mathrm{m}^{-3}$. Li-BES targets densities down to $5 \cdot 10^{17}\,\mathrm{m}^{-3}$ up to 2 cm in the limiter shadow. For LP, data beyond 3 cm in the limiter shadow was excluded, but no lower limit for the density is given.

1.3 Microwave Intensity refractometer in the Limiter Shadow

1.3.1 Theoretical basis of the diagnostic

Microwave Intensity refractometer in the Limiter Shadow (MILS) is the first experimental implementation of a novel diagnostic technique called intensity refractometry (Figure 3) [10]. The electron density is measured by sending a wave in the 'ordinary' mode (O-mode) through the edge of the plasma. The O-mode polarization is achieved by sending the wave perpendicular to the background magnetic field, meaning $\vec{k} \perp \vec{B}$, where $\vec{k}$ is the wave vector and $\vec{B}$ is the total magnetic field. The electric field $\vec{E}$ of the wave must be parallel to the background plasma magnetic field $\vec{B}$, meaning $\vec{E} \parallel \vec{B}$. The dispersion relation for the O-mode is

$$n^2 = 1 - \frac{\omega_\mathrm{p}^2}{\omega^2} \tag{1.4}$$

where n is the refractive index with $n = \frac{c|\vec{k}|}{\omega}$, c being the speed of light and ω the angular frequency of the wave. $\omega_\mathrm{p} = \sqrt{\frac{n_\mathrm{e} e^2}{m_\mathrm{e} \epsilon_0}}$ is the plasma frequency with electron density n_e, elementary charge e, electron mass m_e, and vacuum permittivity ϵ_0 [3]. It can be seen that the refractive index depends only on the electron density and therefore this mode is appropriate for measuring density.

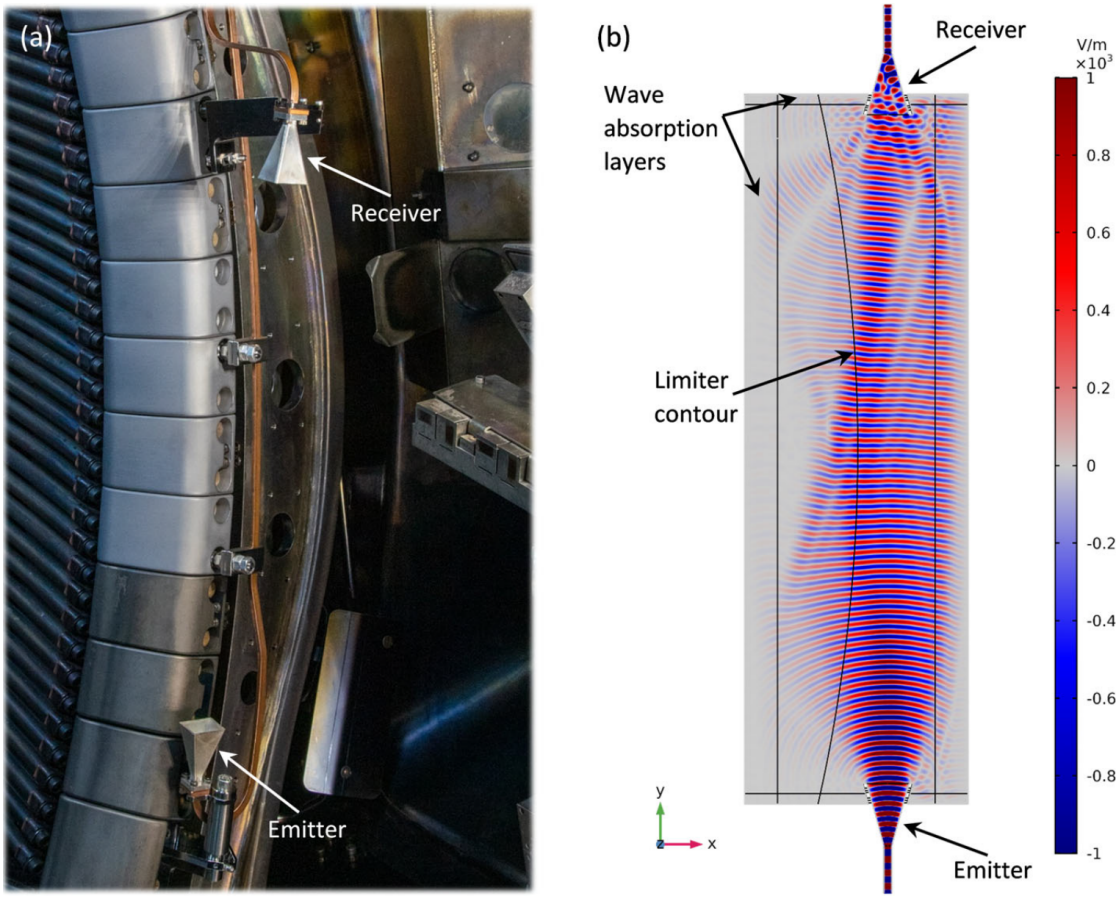

Figure 3: Left: MILS setup inside AUG. Right: a full-wave simulation of the propagation of MILS probing wave in the plasma, its refraction from the high-density region on the left and its interference at the receiver antenna. Figure taken from [11].

In case of oblique incidence, the wave reaches a turning point, which corresponds to the deepest wave propagation in the radial direction, defined by

$$\frac{k^2}{k_0^2} = \frac{k_\mathrm{r}^2 + k_\theta^2}{k_0^2} = 1 - \frac{\omega_\mathrm{p}^2}{\omega^2} \tag{1.5}$$

with a turning point at $k_r = 0$ and density defined from $\omega^2 \cdot (1 - \cos^2(\theta)) = \omega_p^2$, with θ being the angle between the wave vector $\vec{k}$ and the MILS axis.
Thus when the grazing angle is reached ($\theta \sim 0$) the density at the turning point becomes very small $n_{\text{turning}} \to 0$. This explains why MILS is well adapted to probe the far plasma edge with microwaves.

The microwave is sent at 47 GHz through a horn antenna into the toroidal chamber. The wave is received by an identical antenna. The left side of Figure 3 shows the two horn antennas in the torus. The quantities measured and used for the reconstruction of the density profile are the phase and the power of the received wave. More information about these quantities will be given in subsection 1.3.2. The wave going through the plasma is always compared with a wave going through vacuum. Therefore, only values relative to each other are measured.

The right side of Figure 3 shows the MILS probing wave propagation in the plasma, modelled in a 3D full-wave synthetic diagnostic in COMSOL [10]. Not only the waves traveling on a straight line between the antennas are able to reach the receiver but also waves that are refracted from denser parts of the plasma. The measurement region of MILS depends on the density of the plasma and it is up to 5 cm before and up to 5 cm after the limiter. Electron densities in the range from $10^{15}\,\mathrm{m}^{-3}$ to $\sim 10^{19}\,\mathrm{m}^{-3}$ can be probed in the plasma edge. The lower boundary is due to the fact that the change in phase is not measurable below a certain threshold. The upper limit is defined by the diagnostic design parameters, in particular the location and the radiation pattern of the emitter and the receiver and the probing wave frequency.

Due to its high temporal resolution, MILS can detect fast density fluctuations, which can be caused by ELMs or filaments [11]. ELMs are peeling-ballooning MHD instabilities, formed in the pedestal region of the plasma and propagating outwards in the SOL in the shape of cylindrical structures with increased density and temperature elongated along the magnetic field. They appear in the high confinement mode. They can negatively influence the performance of a fusion reactor as they could decrease confinement time and damage wall components. Filaments (blobs) are elongated cylindrical formations of denser and hotter plasma, similar to the ELMs in the SOL, however typically smaller in size and with lower density and temperature.

1.3.2 Experimental Setup

The MILS diagnostic is located in Sector 12 in AUG. A radial-poloidal cross section can be seen in Figure 4.

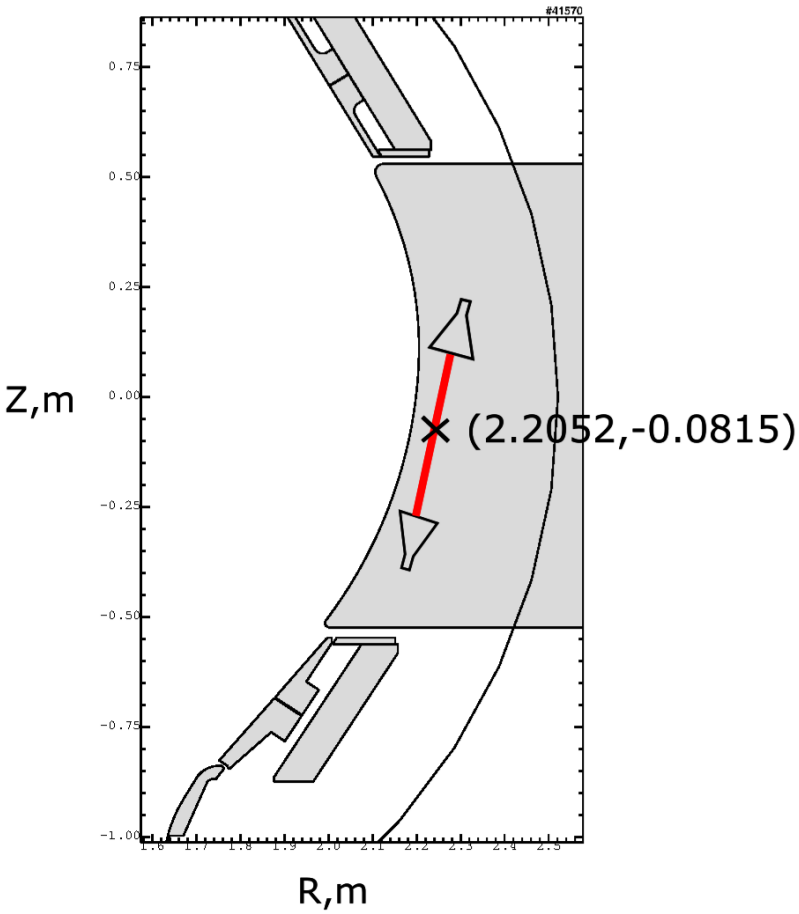

Figure 4: A poloidal cross section of AUG, showing the MILS diagnostics coordinates. The MILS axis is marked in red.

The setup inside the torus can be seen in Figure 3. The shown configuration, with the axis length of 429.1 mm, was used in two AUG experimental campaigns, in 2019/2020 and 2020/2021. The configuration is called MILS 1.0. For the third campaign in 2021/2022, the receiver antenna was slightly shifted and slightly turned towards the plasma, referred to as MILS 1.1. It allowed comparing measurement properties of the diagnostic for different configurations. A thermal shield was installed before the 2020/2021 experimental campaign to minimize the thermal expansion of the diagnostic in-vessel parts, which was observed to influence

the signal. (Figure 5).

Figure 5: On the left side of the figure the MILS diagnostic is shown as used in the year 2020. From 2021 on, a thermal shield has been installed to reduce expansion of the waveguides, as can be seen on the right side. Figure taken from [12].

The antenna holders are connected to the cooling frame of the ICRF (ion cyclotron range of frequencies) antenna, ensuring that the emitter and the receiver positions are well fixed and cannot drift due to thermal expansion.

In Figure 6 the electronic scheme of the MILS diagnostic is shown. The signal is generated at the Kuhne MKU LO 8-13 PLL at 11.736 GHz and 20 mW. This frequency is chosen so it can be transmitted via coaxial cables with SMA connectors. Two Kuhne MKU 47 G2 transverter modules, visible as "f x 4", are used as Transmitter and Receiver. The frequency of the signal is multiplied by four in these modules, resulting in 46.944 GHz. Additionally 145 MHz are fed into the Transmitter resulting in an intermediate frequency of 47.089 GHz sent through the plasma. This signal is generated by the dual channel signal generator Siglent SDG

6022X. The modulation and detection of the signals is also done at 145 MHz.
One signal goes through the "vacuum path" directly from the transmitter to the phase detector, giving a reference signal. The second signal is sent through one of the antennas, probing the plasma, and is then collected by the other antenna. This is the so called "plasma path".

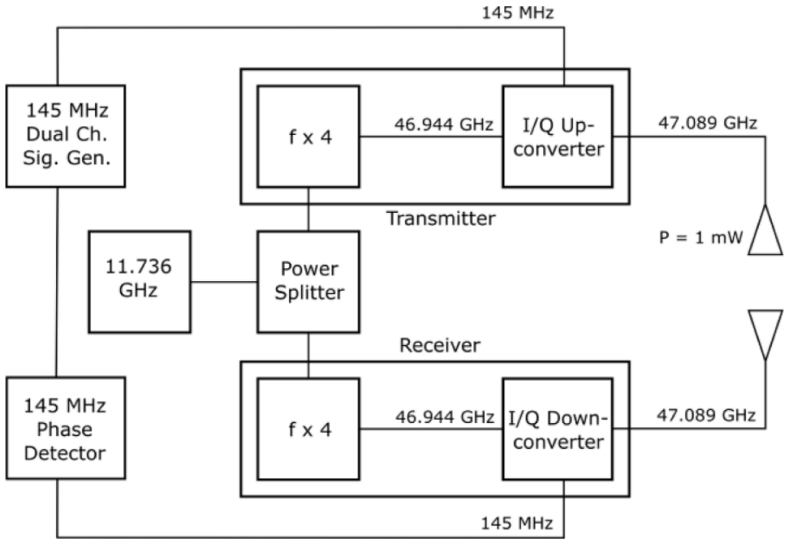

Figure 6: The electronic scheme of the MILS diagnostic. It is further described in the text. Figure taken from [12].

Two quantities of the received probing wave are measured, the power and the phase. For the phase, a relative value is measured between the "plasma path" and the "vacuum path". To enable a measurement of the phase differences of up to 360°, the received wave is split into two parts, where one undergoes a phase shift of 90° in the employed detector (Figure 7).
The power sent at the antenna through the plasma is about 1 mW. The power received varies very much depending on the density as can be seen later in chapter 2. In the 2021/2022 experimental campaign, the receiver antenna was tilted towards the plasma and therefore much higher values of power were measured in this campaign. The power sent through the vacuum path is set to 0.03 mW, being equal to the vacuum power level of the plasma path.

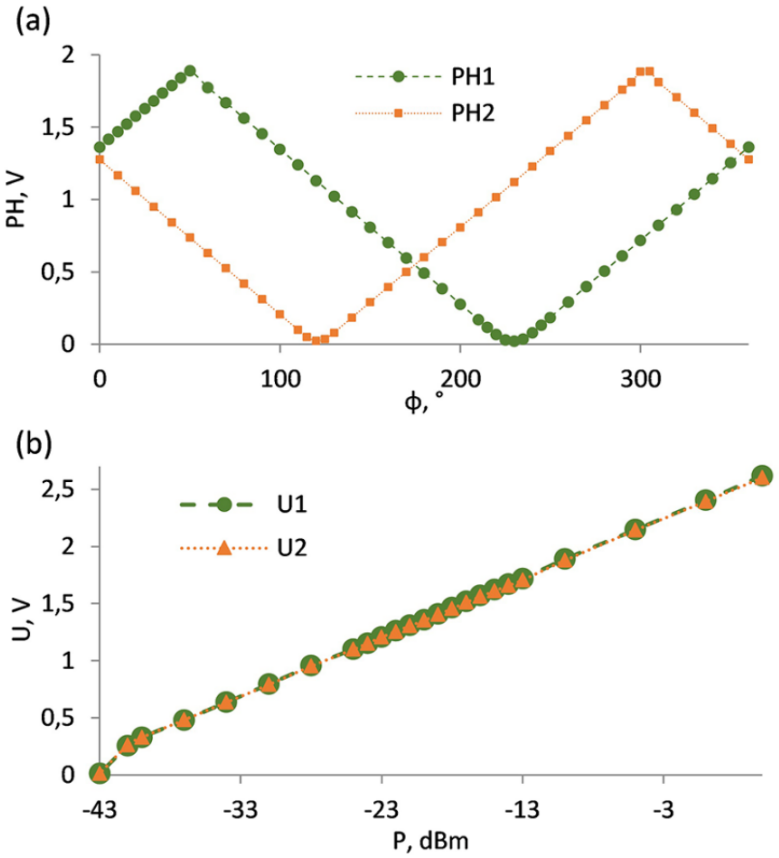

Figure 7: The calibration curves for the different signals. A phase shift of 90° is done in (a) to ensure the possibility to measure a phase differences of 360°. In (b) the respective curves for the power U1 and U2 is shown. Figure taken from [12].

MILS measures four different signals, PH1 (phase of the signal in the plasma path), PH2 (shifted phase of the signal in the plasma path), U1 (power of the signal in the vacuum path) and U2 (power of the signal in the plasma path). The correspondence of the raw data in V to the absolute values of phase in deg and power in dBm can be seen in the calibration diagrams in Figure 7. In most of further applications, the measured power is set relative to the vacuum power, meaning $\frac{P}{P_{\text{vac}}}$.

An example of how these signals can look during a plasma discharge can be seen in Figure 8

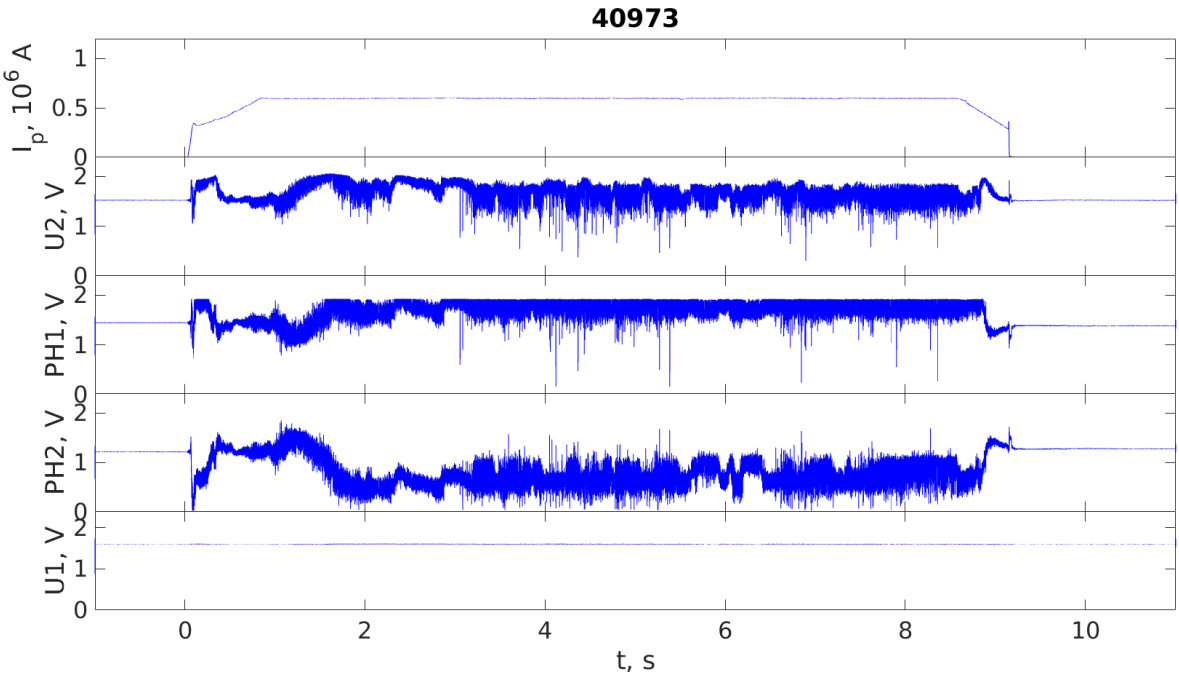

Figure 8: An example of the measured signals during a given plasma discharge 40973. The plasma current is visible in the top.

In the top of the figure the plasma current can be seen with a stable plateau from $\sim$ 1 s until $\sim$ 8.5 s. During this main phase, a slow density evolution as well as fast oscillations are observed by MILS. Both power and phase are affected significantly by the density changes.
After collecting PH1, PH2, U1 and U2, which are referred to as raw data, the data is processed (section 2.1). After processing the raw data, it gets calibrated (subsection 2.1.3) and then processed again (section 2.2). With this final data, density reconstruction can be done.

1.3.3 Density reconstruction

In some cases, direct correlation between the measured quantity and the desired quantity is given. Regarding MILS, no direct connection between phase and power of a microwave and the density is known. Therefore, to be able to reconstruct a density profile from experimental points, forward modeling is needed beforehand. Since this is a novel diagnostic, data interpretation was developed from scratch. The forward model is done as full-wave 3D modeling in COMSOL commercial

software [10] [13].
In the model, the exact geometry of the MILS horn antennas and their location is implemented (see Figure 3). The plasma is described in the cold plasma approximation [14]. In the experiment, the density varies in all three dimensions. The model is capable of using 3D input density. However, for simplicity some assumptions are made. The first assumption is a constant density profile along the magnetic field lines. This is valid for this application as the size of the measurement region in this direction is small and parallel transport in the SOL is typically many orders of magnitude higher as cross-field transport [15]. Second, in poloidal direction, the density is assumed constant along the flux surfaces, and the experimental flux surfaces are closely represented by circular shape in the model. The third assumption for modeling is an exponentially decaying density profile shape in radial direction with different slopes before and after the limiter. It is shown in Figure 9.

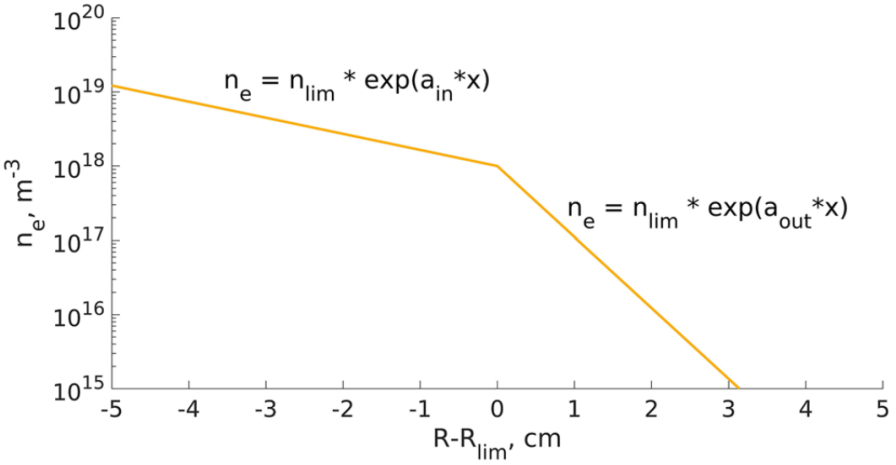

Figure 9: The radial plasma density assumed for the modeling. Before and after the limiter an exponential decay of the electron density is presumed, being only different in the slope. The y-axis is plotted logarithmically. Taken from [10].

In the model, the density input is varied within the range of typical values observed in AUG. Different densities result in different values of phase and power, which can be observed in Figure 10. The whole set of modeled cases constitute the database, which then can be used to obtain density values from phase and power measured in the experiment.

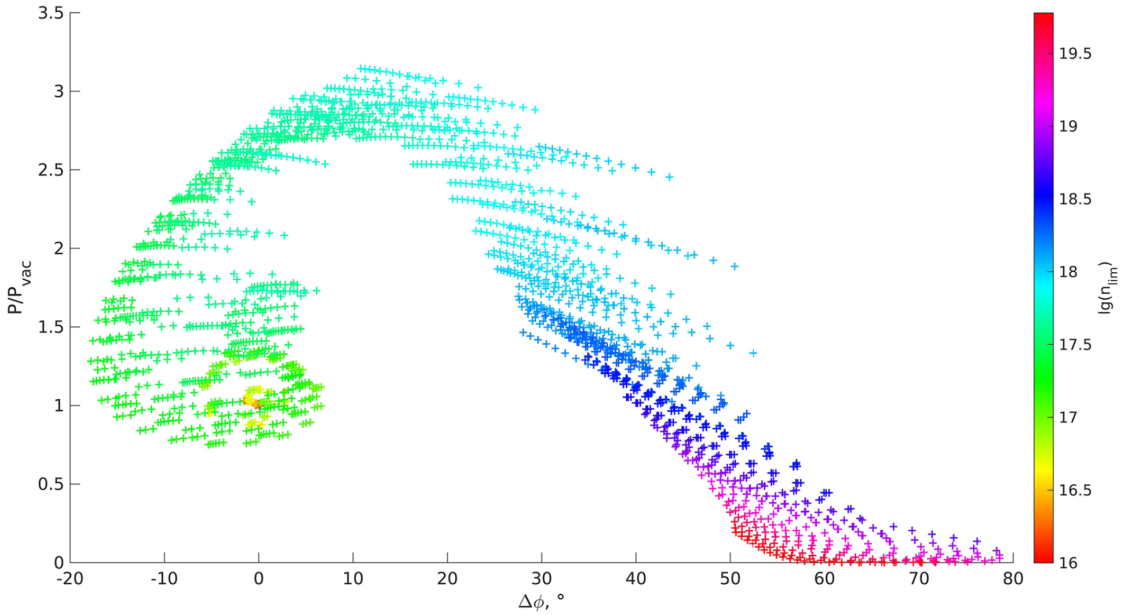

Figure 10: The dependency of the ratio of power from phase difference as a result from the modeling approach for MILS 1.0. The different colors indicate different densities at the limiter. Taken from [10].

A specialized algorithm called genMILS [10] is introduced to reconstruct a density profile. It takes modeled points in the range of $3\delta\varphi$ and $3\delta P$ next to experimental points, where $\delta\varphi$ and δP are error bars for the experimental points. Each chosen point is assigned a weight defined as the Akaike weight [16] under the assumption of Gaussian distribution of δP and $\delta\varphi$. The Akaike weight w is a measure that quantifies the relative likelihood of different models being the best fit for a given set of data. In our case it is defined as

$$w = exp\left(-\frac{(\varphi-\varphi_{\text{input}})^2}{2\delta\varphi^2} - \frac{\left(\frac{P-P_{\text{input}}}{P_{\text{input}}}\right)^2}{2\delta P^2}\right). \tag{1.6}$$

The density profile is determined by calculating the density at several radial points independently by the equation

$$n_{\text{e}} = \frac{\sum_i n_{\text{e}_i} \times w_i}{\sum_i w_i}, \tag{1.7}$$

n_{e_i} being the density value at a specific radial position in the profile i and w_i the weight of this profile. For each radial point the corresponding error is also calculated independently.

In Figure 11 a few example points are taken for density reconstruction. For every point marked in black, the surrounding points selected for density reconstruction are shown in color corresponding to their weight. In this example, $\delta\varphi = 1$ and $\delta P = 3\%$ are taken as representative for the expected order of magnitude. The results for the density profiles are shown in Figure 12. The variation of the error is between 5% and 15% in this example.

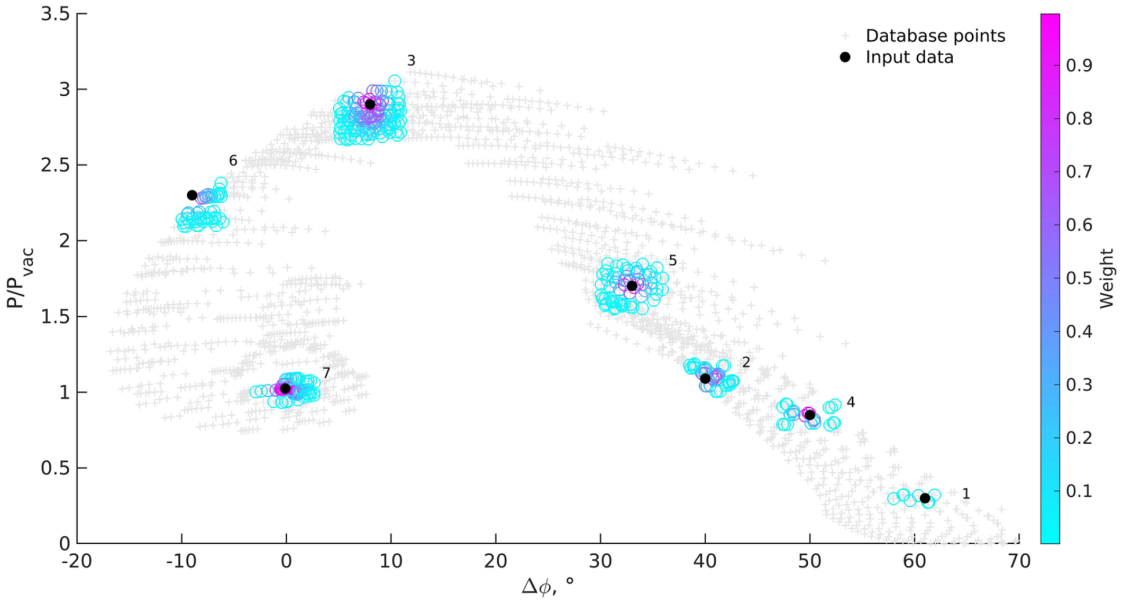

Figure 11: The database gained from modeling in grey with a few points marked in black taken as input points for density reconstruction. Different density profiles surrounding the input points are contributing with different weight to the resulting density profile. Taken from [10].

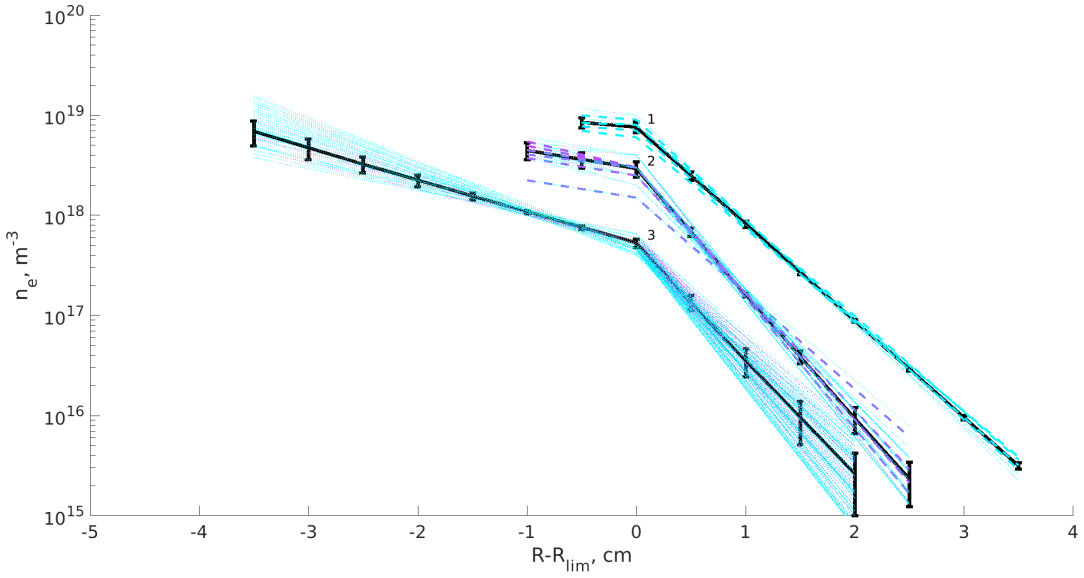

Figure 12: Several example radial density profiles obtained for some of the input points in Figure 11. Taken from [10].

1.4 Motivation and work structure

As mentioned before, densities in the limiter shadow and in the few *cm* in front of the limiter are often poorly diagnosed. MILS allows obtaining measurements of the electron density in this region, with high temporal resolution and good accuracy [10]. In order to reconstruct the density profile from experimental signals, a reliable data analysis algorithm has to be established and validated. The presented work focuses on the validation and improvement of the data processing techniques, used for MILS experimental data and partially described in [12] and presented in details here.

There are different factors that can distort MILS data or lead to the need of special processing of the data:

- Power outage due to high stray magnetic field close to MILS electronics
- Large density fluctuations
- Signal drift during a discharge due to thermal expansion of in-vessel waveguide parts

In some cases, a large current in specific coils leads to power outages of the MILS power supply. These outages have be identified and cut from the signals

(see subsection 2.1.1).
In order to ensure correct evaluation of the density in the presence of large density perturbations (ELMs and large filaments), these perturbations are carefully removed from the signal with an algorithm described in subsection 2.1.2. During the calibration of data an analysis for the phase measurements in respect to the calibration curves is done (subsection 2.1.3).
It was found that heat loads from the plasma lead to thermal expansion of some of the in-vessel components of MILS. MILS signal drifts due to this expansion have to be corrected. This is further explained in subsection 2.2.1.
Afterwards the calibrated and processed experimental data is compared to the database of a MILS synthetic diagnostic. Potential discrepancies between the results will be discussed in section 2.4.

2 Data Processing and Analysis

In this chapter the processing of the raw signals is described. Afterwards the calibration of data and the further processing of the calibrated data is presented. A comparison between experimental and synthetical values is done and finally a density reconstruction from the calibrated data is depicted with comparison to other diagnostics. Only parts of the signals during stable plasma current conditions are taken into account for the further data processing and analysis.

2.1 Processing of raw data

The four different signals (two phase signals PH1 and PH2 and two power signals U1 and U2), introduced in subsection 1.3.2, are collected in Volts coming directly from the MILS detector.
The data acquisition was done at 2 MHz throughout the different experimental campaigns. Until the middle of the 2021/2022 experimental campaign (until the shot 40652), the signal detection included a 100 kHz lowpass filter, which reduces the meaningful range of the frequencies in the signal to 200 kHz. Therefore, the data is downsampled by a factor of 10. For the shots from 40652, in this work the same downsampling is applied as well, to reduce data processing time without consequence on the actual MILS measurement.

2.1.1 Power outages

As briefly mentioned before, it was noticed that some electric components switched off in some plasma discharges, when high stray magnetic field was present. Looking further into detail, the DC-DC converters in the Kuhne MKU 47 G2 transverter modules tripped, if the current in the AUG V3 coils, which are closest to the MILS electronics, exceeded a certain level. Temporal loss of the MILS signal was the consequence. It is visible in the signals as a prolonged drop of power to a very low constant level (see Figure 13). To prevent further incidences, the DC-DC converters were bypassed and the supply voltage was changed from $12 - 14\,\mathrm{V}$ to $5.2\,\mathrm{V}$, as instructed by the manufacturer [12].

In order to ensure the use of the unaffected parts of the signal for data analysis, discharges with power outage had to be identified and the parts of the signals, where the power dropped, had to be removed. An algorithm was created to check, if the mean value of power dropped below 0.6 V for a period of at least 5 ms. The algorithm removes these parts with a constant buffer of 1 ms before and 10 ms after the found region to make sure to remove all the affected data, also in transition regions. The values were chosen to make sure that the drop was not the result of fast density changes.

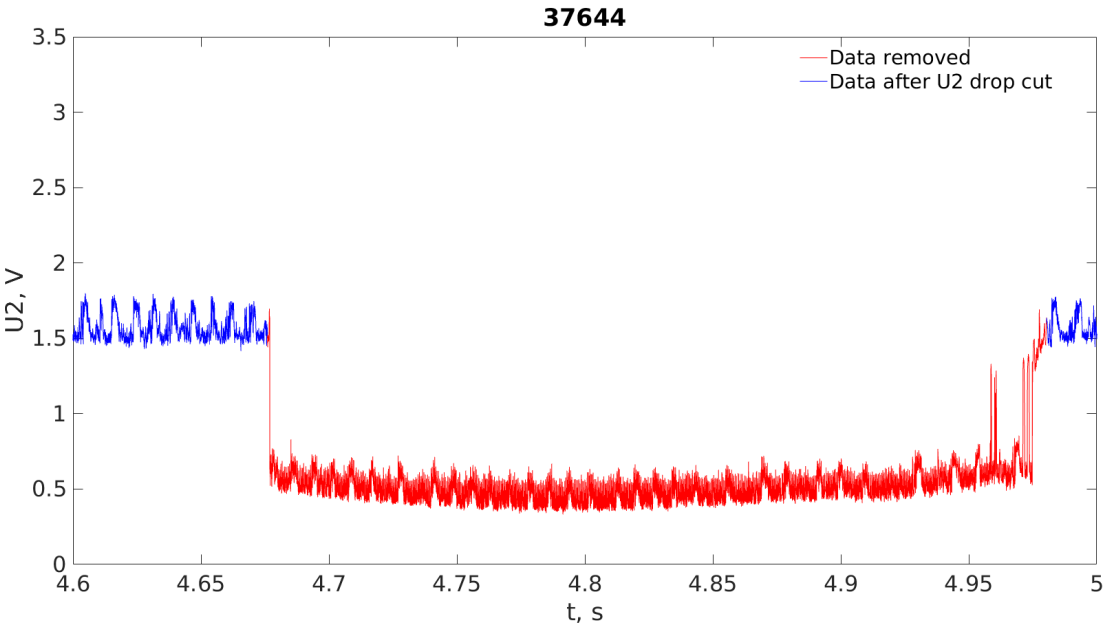

Figure 13: A drop due to power outage is visible in the raw U2 signal of discharge 37644. It corresponds to power outage due to high stray magnetic field close to MILS electronics. The data removed is visible in red, the remaining data in blue.

2.1.2 Removal of ELMs and oscillations

Accurate removal of ELMs and oscillations, induced by drastic transient changes in the density profile, from the MILS signals was a major focus of this work. ELMs are observable in the MILS signals as large and fast oscillations in both phase and power, which are followed by the signal going back to the pre-ELM level after the ELM has passed. Both can be seen in Figure 14. The observations show, that MILS is able to follow the ELM time-evolution in phase and amplitude. However, these perturbations need to be removed to ensure a meaningful background density profile reconstruction. At the same time, MILS signals are very sensitive to changes in the density profile and therefore it is possible to study those changes in more detail. This work however will not focus on their analysis. However, not in all discharges ELMs are as clear as in Figure 14. Figure 15 shows an example of a discharge with many oscillations in a small time window. The algorithm described below is applied to all type of ELMs in the same way. Its validity for different types of oscillations is discussed afterwards.

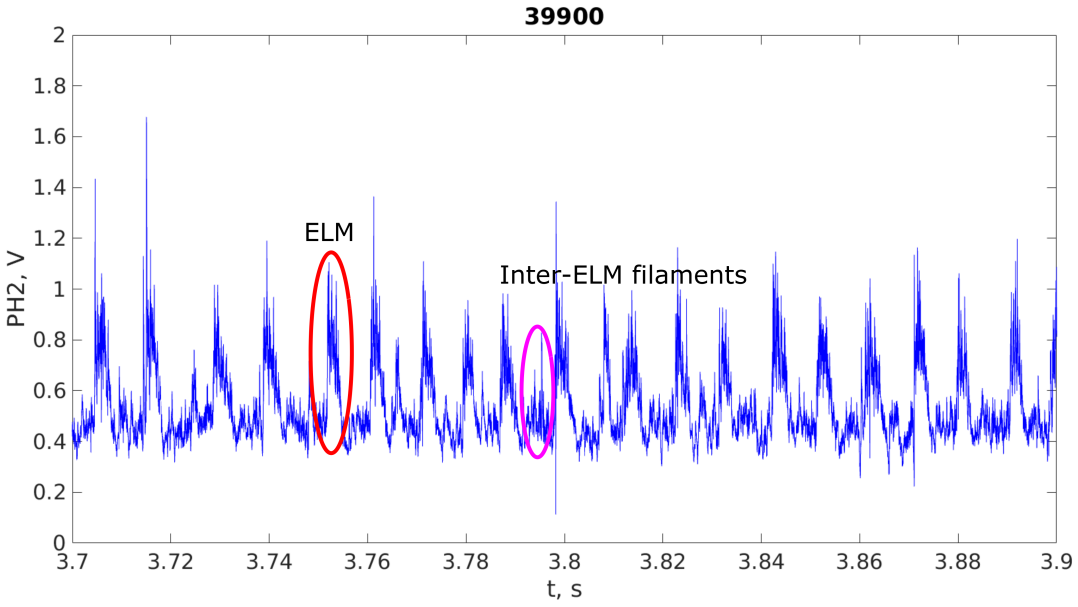

Figure 14: Time interval of 3.7 s to 3.9 s of the PH2 signal of discharge 39900. This shot is a H-mode with type-I ELMs. The ELMs are visible in the signals, one of them marked in red. An example of Inter-ELM filaments is marked in magenta.

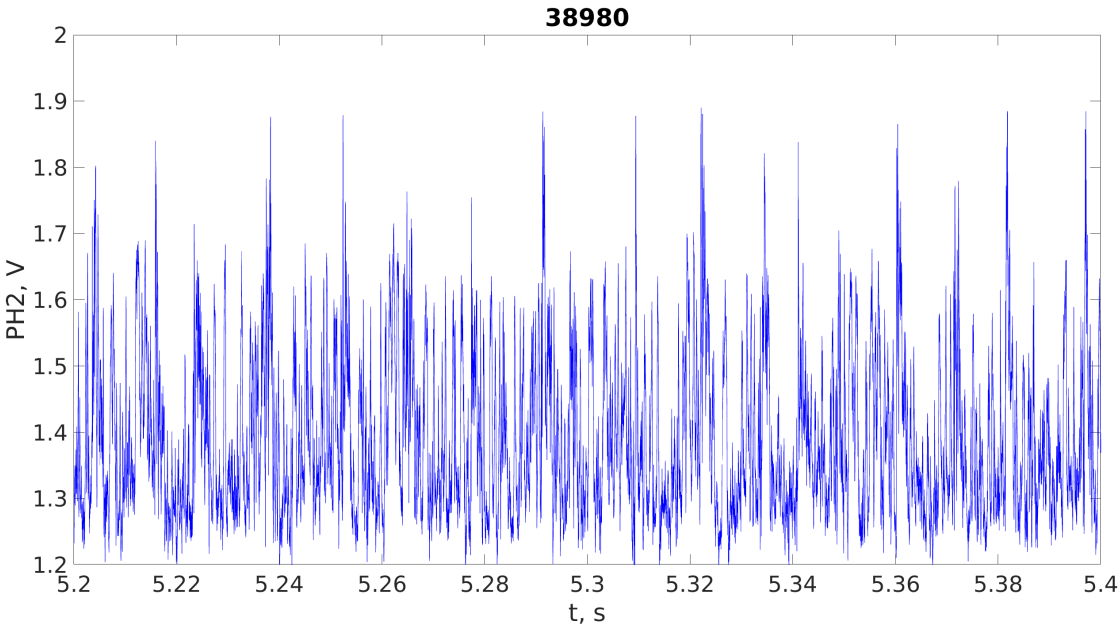

Figure 15: The figure shows the PH2 signal of discharge 38980 from 5.2 s until 5.4 s. Many oscillations are visible, which makes the detection of ELMs and filaments more difficult.

The algorithm removing ELMs and fast oscillations consists of several parts. The first processing step is based on a signal called "ELM", that contains information about the timestamps of the ELMs during plasma discharges. The timing of ELMs in the "ELM" signal is calculated based on the currents measured by shunts in the divertor of AUG, and in some cases bolometer measurements are used. The algorithm used to detect the ELMs is based on a method called automatic multiscale-based peak detection (AMPD) [17]. However, in this work it was observed that this processing step does not allow complete detection of all ELMs and their full duration. Very often only part of the perturbations were found. Therefore, a constant buffer of 0.1 ms before and 0.3 ms after the initial ELM time was introduced. The parameters were found empirically, looking at different discharges. The constant buffer worked well for many discharges, but not for all (see Figure 16). It is visible that the constant buffer helped, but was not sufficient enough to identify the whole perturbation.

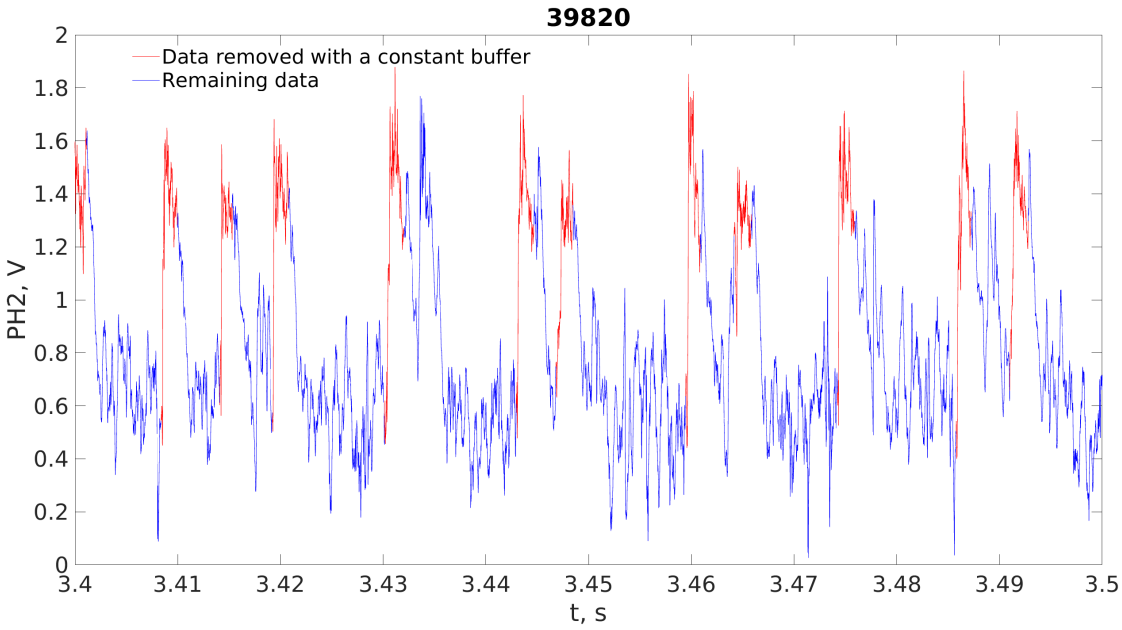

Figure 16: The signal PH2 in specific time window of discharge 39820. In this discharge, the cutout with a constant buffer is not reliable enough, as part of the perturbations remain in the signal.

Therefore, a second part of the ELM removal algorithm was developed, in addition to this constant buffer, a variable buffer was created. It is based on the derivative of the signal before and after an ELM. Four time intervals of 0.5 ms before and after the ELM with constant buffer are analyzed by going from the closest to the farthest. If the absolute value of the mean derivative is above $0.0013\,\frac{\mathrm{V}}{\mathrm{s}}$ in one of the four intervals, the cutout is extended to include the part up to this interval. A figure of the mean derivative in the intervals is shown in Figure 17. In this case, the cutout would be extended to the last interval, as the last mean derivative is below the lower threshold.

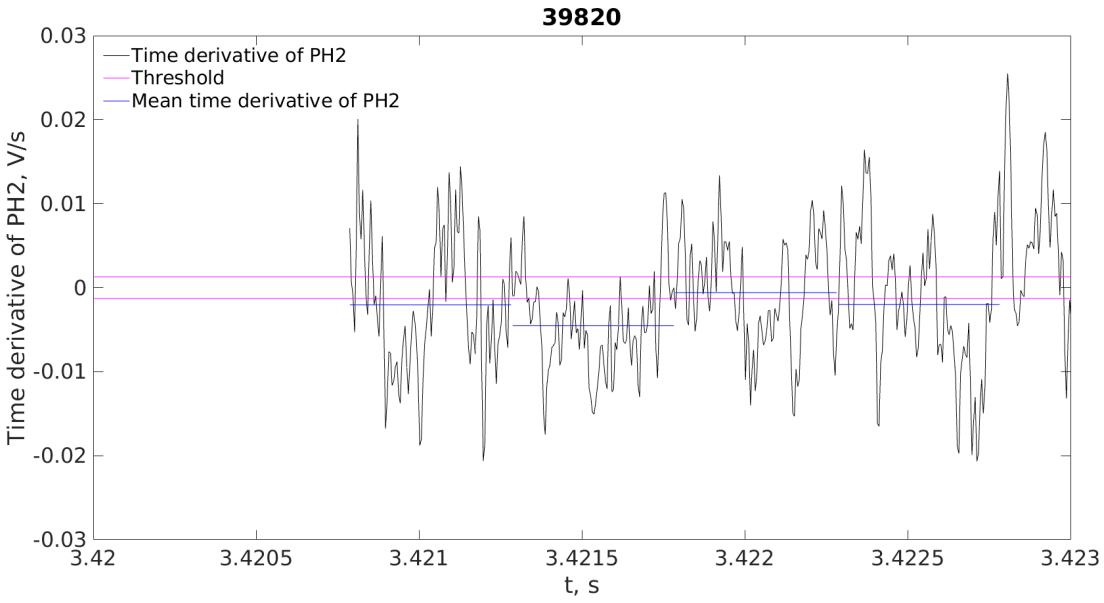

Figure 17: The time derivative of PH2 with respect to the time. The threshold for the algorithm is marked in magenta, the mean time derivative for the single intervals is marked in blue.

After applying the algorithm (Figure 18), most parts of the ELMs are detected correctly.

Naturally, this algorithm does not work perfectly for every shot, as it depends on how well the initial ELMs are found in the "ELM" signal, that is used. Additionally it depends on the ELM properties, like duration and frequency. Especially for discharges with small ELM duration in a very short period of time the algorithm removes too much data. Therefore it can be improved by making the length of the time intervals or the amount dependent on the initial ELM length or ELM frequency. This is not part of this work and needs to be investigated further.

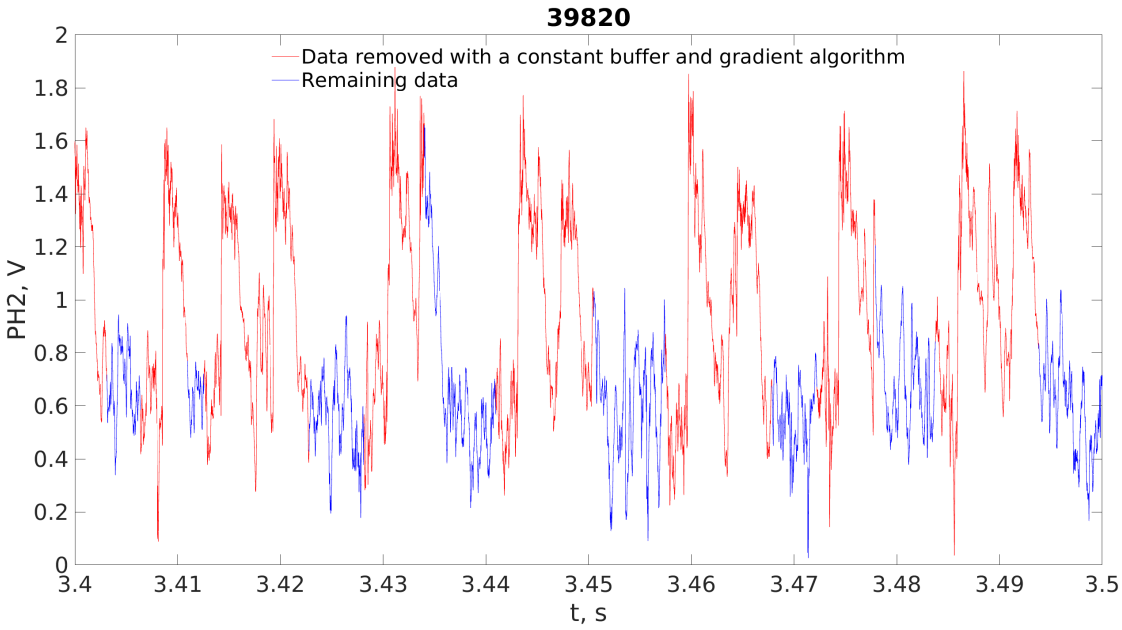

Figure 18: The same data as in Figure 16, but after applying the algorithm based on the derivative of the signal. Most of the perturbations are detected correctly.

While the described first two steps of the ELM removal algorithm allow sufficient processing in most of the discharges, it was noticed that not for every discharge with useable MILS data ELM data is available. For this reason the third part of the algorithm was created. It splits the data into i intervals of length 20 ms, calculates the mean value μ_i and the standard deviation σ_i and removes points which are outside $\mu_i \pm 2.5\sigma_i$. This time window size is chosen long enough to make sure that the mean value is not dominated by strong oscillations but rather by the background signal. The 2.5σ criterion is commonly used when removing fast oscillations [18]. This part of the algorithm is applied to the discharge even if the "ELM" shotfile is available. This ensures the removal of large oscillations and parts of ELMs that are not detected in the "ELM" shotfile.

An example of a final result of raw data after the three steps of the ELM removal algorithm can be seen in Figure 19. The different algorithms are applied to PH1, PH2, U1 and U2 individually, but to ensure the further use of the signals, the cutout is synchronized after each algorithm. Synchronization is done by cutting the same data points automatically from all signals, if they are removed in any signal.

A discharge, where no "ELM" signal is available and only the third part of the

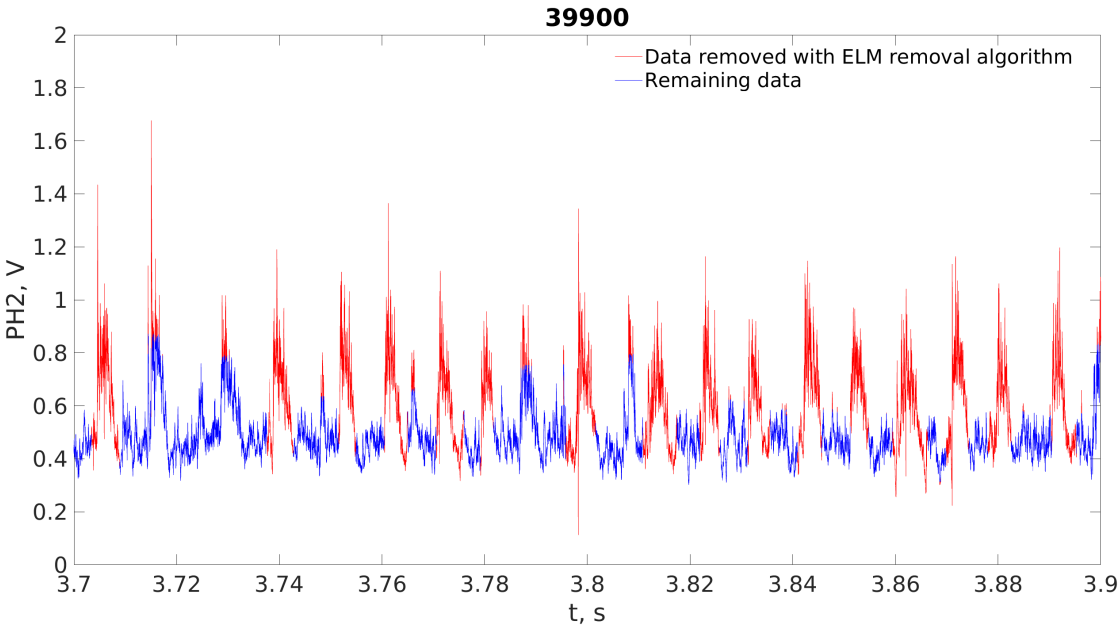

Figure 19: Time interval of 3.7 s to 3.9 s of the PH2 signal of discharge 38186. Data that is cut from the original signals is highlighted in red, the remaining data in dark blue. Here, only the third part of the ELM removal algorithm can be applied.

ELM removal algorithm is applied, can be seen in Figure 20. As can be observed, many parts of the signal, which normally would be counted as an ELM, are not entirely removed from the signals. In this particular case, the density perturbations are very fast.

It can be said that, when only the third part of the algorithm is applied, fast oscillations are cut correctly. However, the removal of bigger perturbations like ELMs is not entirely possible, as the third part of the algorithm would only remove the upper part of the ELM and not the whole perturbation. If necessary, the third part of the ELM removal algorithm could be combined with the second part of the algorithm to check intervals around the cut-out fluctuations.

2.1.3 Calibration and analysis of raw phase signals correlation

In order to obtain the absolute values of the measured phase and power variation, a calibration to phase in degrees and power in decibel-milliwatts (dBm) has to be done. The power, measured in Volts, is converted to dBm with a linear fit

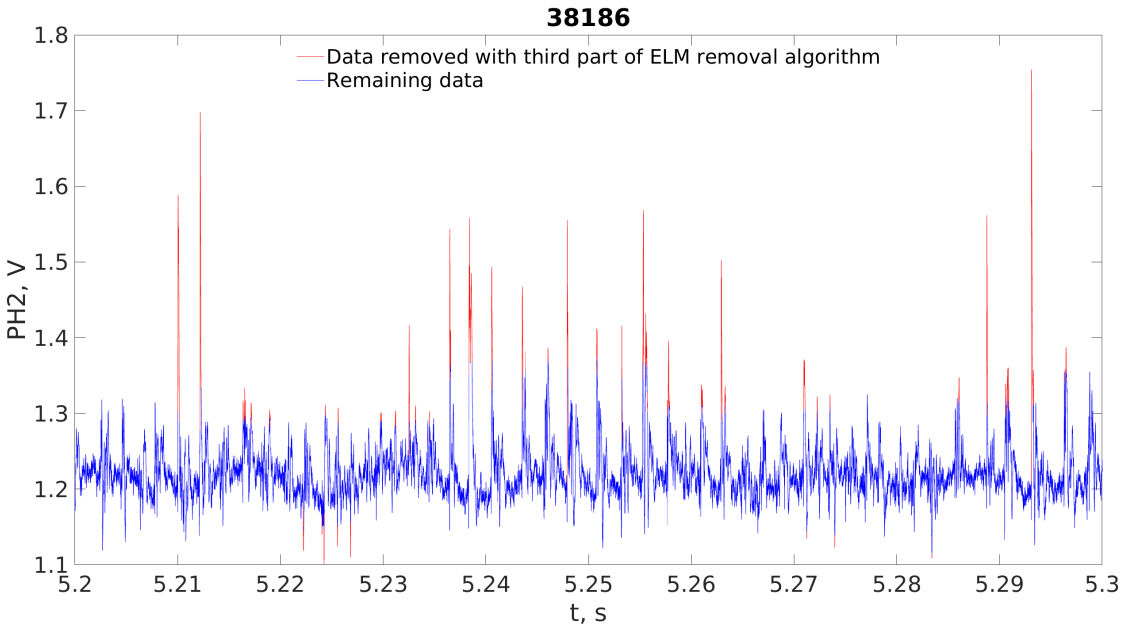

Figure 20: A small time interval of the PH2 signal of discharge 38186. Data that is cut with the third part of the algorithm is highlighted in red, the remaining data in dark blue. Strong oscillations are removed.

(bottom part of Figure 7). The values of the phase in degrees are obtained by using both the PH1 and PH2 signals. The non-linear "corner" regions are avoided and only the linear parts of the calibration curves (Fig. 7b) are used for the phase evaluation. The error in power can only be characterized by the noise level in the vacuum signal. It was found to be 1.7 mV, which corresponds to 0.8%. The estimation of the error in phase is described below.

During the phase calibration process, it was noticed that some data cannot be recalculated unambiguously from PH1 and PH2 to values in degrees. While both PH1 and PH2 values should correspond to the same value in degrees, various noise sources distort the PH1 and PH2 signals in different ways, which lead to discrepancies between them.

This can be illustrated in a PH2-PH1 plot, where the calibration curve shows the line, on which all the measured values should lie in the absence of any distortion, and the experimental data exhibits deviations from this curve (Figure 21). From the experimental data, it was observed that most of the points lie within the deviation of 0.02 V, corresponding to 2°, which defines a typical value of the phase error. Points that deviate more than this value, are considered to be out of range or 'outliers'. The error is caused by several factors, including noise in cables and electronics, ICRH power and density perturbations like ELMs or filaments. Some

of the factors are analyzed below.
First, the influence of the density perturbations is studied. In Figure 21, an example of PH1 and PH2 data from one AUG discharge is shown before and after applying the ELM removal algorithm (all three parts of the algorithm applied). Before ELM removal, the percentage of points out of range was 0.53%, which decreased to 0.15% after applying it. After analyzing many shots, it was observed that perturbations in density cause points out of range.

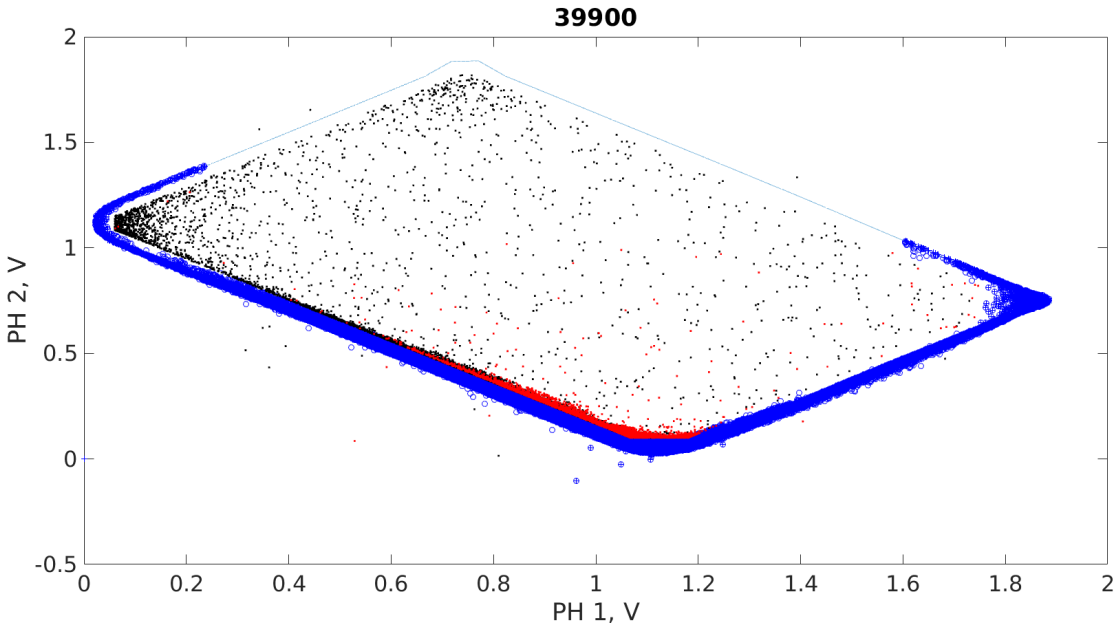

Figure 21: A comparison between the data in respect to the calibration curve before and after applying the different algorithms. The blue points show the data in the errorbar range of the calibration curves. The black points indicate the data out of range before applying the algorithm and the red points the remaining data out of range after applying the algorithm.

Most of the black points, that are points out of range, are removed with the algorithm. However, it has to be said that not only points out of range are removed with the algorithm, but also points that are next to the calibration curves. In most cases, the percentage of points out of range dropped nevertheless or stayed at least almost constant.

On the other hand, one has to differentiate between discharges that go through each step of the ELM removal algorithm or discharges, where only the 2.5σ criterion is applied. The discharge in Figure 21 undergoes all steps in contrast to Figure 22 , where only the last part of the algorithm is applied.

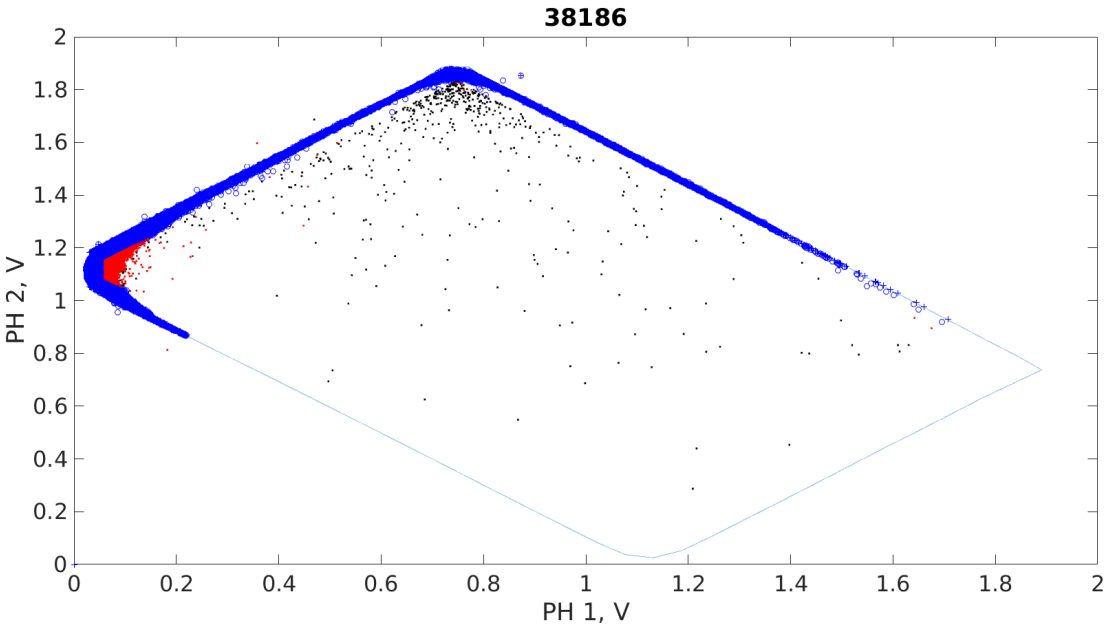

Figure 22: The colors indicate the same as in Figure 21. Here, the removal works pretty well, even though this discharge only goes through the third step of the ELM removal algorithm.

Nevertheless, it can be noticed that the amount of points out of range decreased significantly. This is due to the fact that points far from the calibration curve are often found in spikes in the signals, which are removed with the third part of the ELM removal algorithm. In this case, the percentage of points out of range went from 9.03% to 8.97%, yielding again that not only points out of range are removed. On both Figure 21 and Figure 22 points out of range, marked in red, remain. These remaining points are now analyzed in the following.

Not all points too far from the calibration curves correspond to ELMs or oscillations. It was observed in many cases, that outliers from the PH2 over PH1 calibration curve correlate with the ion cyclotron resonance heating (ICRH) power. When a certain threshold of power was reached, the ICRH caused points far from the calibration curve. However, it was not possible to find a clear value for this threshold. The correlation between the quantities observed during a discharge can

be seen in Figure 23. The reason for this correspondence most likely is the phasing of the ICRH antennas. In the time intervals, that correspond to the points out of range, the phasing, which is further explained in section 2.4, was different then in the other time intervals, where no outliers are present. In the time intervals with no points deviating the phasing was set to dipole phasing, meaning the current in the neighbor antennas straps is in opposite direction, which minimizes effects on the plasma near the limiter [22].

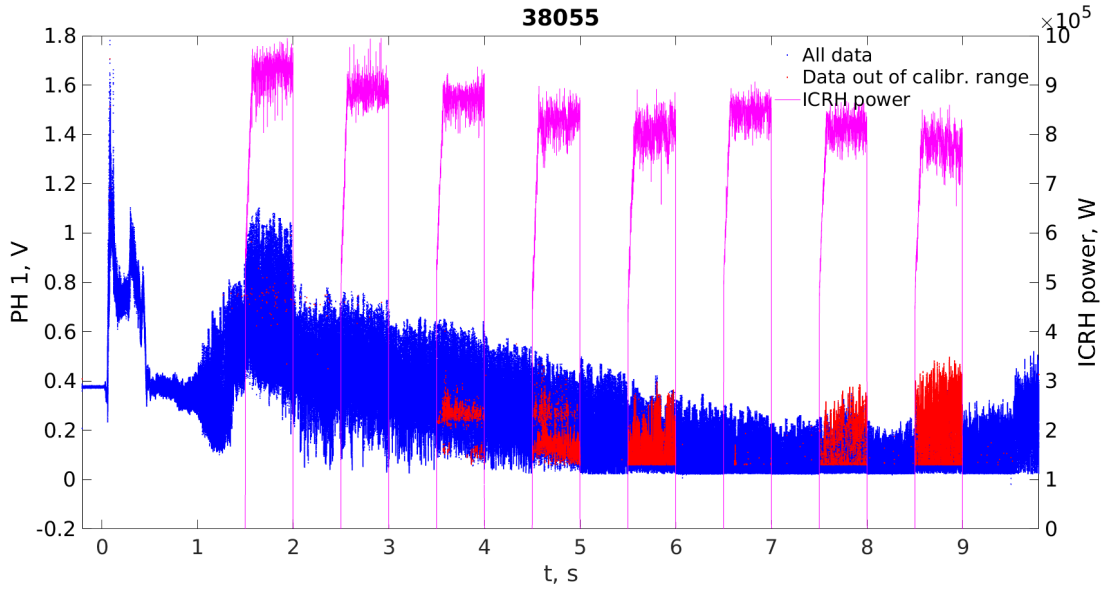

Figure 23: A comparison between the remaining points out of range and the ICRH power. Very good correlation can be seen between the signals.

A possible improvement on discharges, where the "ELM" signal is not available, could be done by applying the second part of the ELM algorithm after the removal of peaks and strong oscillations. This would remove further steep parts of the signals next the already removed peaks. This idea can be considered for future improvements.

2.2 Processing of calibrated data

After the phase and power signals are calibrated to the absolute values, further processing is required before density reconstruction can be done. The processing contains the consideration of the expansion of the in-vessel components and the correction of the associated effects. Additionally, errors caused by the data processing described in this section, are evaluated and summarized in section 2.3.

2.2.1 Thermal expansion

The most influential factor for the processing is the signal drift during a discharge, caused by the thermal expansion of the in-vessel parts. It depends mostly on the total energy radiated during a plasma discharge as found in [12]. Both the phase and power show almost a linear dependency on the radiated energy, as can be seen in Figure 24. As already mentioned in subsection 1.3.2, a thermal shield was installed between the 2019/20 and 2020/21 experimental campaigns. This reduced the thermal expansion and consequently the phase and power drift. The phase drift diminished by the factor 2.6 and the power drift by 2.3 [12].

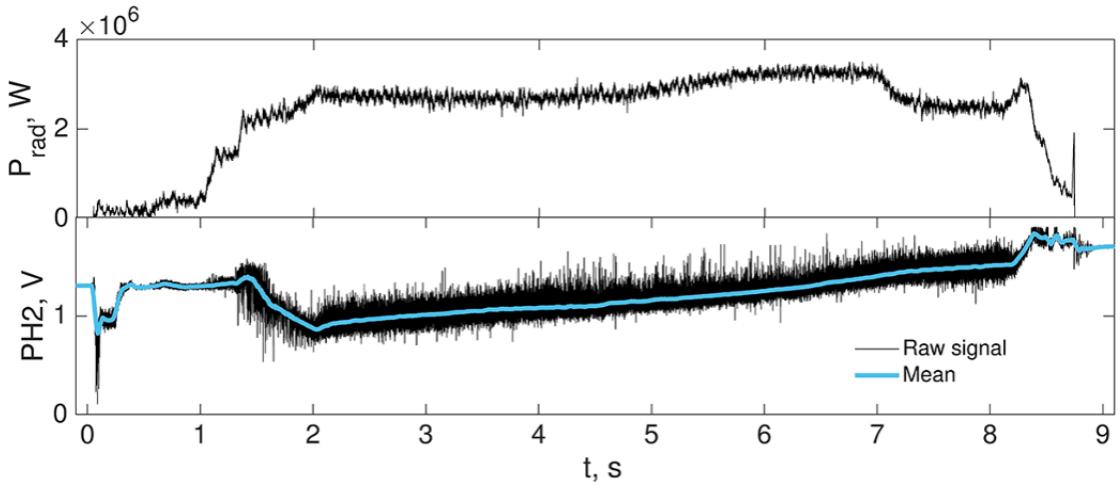

Figure 24: Example of one of the phase signals during a plasma discharge. An almost linear correction due to the thermal expansion can be seen. Taken from [12].

For the correction of the drift, several quantities have to be computed. First of all, the total drift has to be known. It is determined by subtracting the phase or power after the plasma discharge from the ones before the plasma discharge. The signals before the discharge are easily calculated by taking the mean value of the signals 0.2 s before the plasma current rises. Finding the point in time after the discharge is not as trivial and is described in more detail in last part of this section. After finding the point in time after plasma t_{ap}, an average of the signals over $t_{\mathrm{ap}} + 0.1\,\mathrm{s}$ is taken. To find a time dependent correction of the drift, an linear dependency of the drift in respect to the radiated power is assumed. The linear function can be written as

$$\varphi_{\mathrm{corr}}(t) = \frac{\varphi_{\mathrm{drift}} \cdot Q_{\mathrm{cum}}(t)}{Q_{\mathrm{rad}}} \tag{2.1}$$

where $\varphi_{\text{corr}}(t)$ is the time dependent drift, φ_{drift} the total drift, $Q_{\text{cum}}(t)$ the time dependent cumulative radiated energy and Q_{rad} the total radiated energy during the whole discharge. As the real dependency of the drift on the radiated energy might not be linear, an error in phase $\delta\varphi_{\text{drift}}(t)$ and power $\delta P_{\text{drift}}(t)$ is introduced as a function of Q_{rad} based on the RMS of the residuals. It resulted in an error up to 10°in phase and 5% in power before and 3°and 2.5% after installation of the thermal shield.

As mentioned above, finding the point in time labeled as 'after plasma' t_{ap}, is not easy. For this, four different criteria are applied sequentially. First, the decay of the plasma current is taken to determine an initial time. The point where the current first drops below $0.05 \cdot 10^5$ A is taken. Second, the current of the nearest magnetic field coil COIo has to be low enough as it disturbs MILS measurements. Third, any oscillations caused by any other factors are checked. If the oscillations are too high in amplitude, the t_{ap} is shifted until the oscillation amplitude are below a certain threshold. Fourth, it is checked that also no slow variations remain in the signal, so the signal mean ahead of t_{ap} has to be constant within 0.05 s.

2.3 Errors in phase and power

To further use the calibrated data for density reconstruction, the errors in phase and power have to be known, to calculate the errors in the density. There are a few factors that contribute to an error in phase and power, which are summarized here.
First, a noise level of 2°, was observed during the calibration of the phase raw data, which can be caused by several sources as described in subsection 2.1.3. For the raw power data, only the level of the noise in vacuum can be defined, which was found to be 0.8%.
Second, it was noticed that the error in phase $\delta\varphi_{\text{diff}}$ rises drastically when relative power levels below 0.05 are reached. In this case, only a small part of the probing wave is detected by the receiver and noise dominates the signal. Therefore, a broad variety of phase values are possible at low power level and such data cannot be used for the density reconstruction.
The last part of the error in phase and power, as mentioned before, come from the correction for the phase and power drift $\delta\varphi_{\text{drift}}(t)$ and $\delta P_{\text{drift}}(t)$, which are time dependent because the radiated energy is time dependent. The formulas for calculating the errors in different campaigns are $\delta\varphi_{\text{drift}} = 0.17\varphi_{\text{drift}}$, $\delta P_{\text{drift}} = 0.0096 P_{\text{drift}}$ for the 2019/2020 campaign and $\delta\varphi_{\text{drift}} = 0.125\varphi_{\text{drift}}$, $\delta P_{\text{drift}} = 0.0109 P_{\text{drift}}$ for the 2020/2021 campaign, where φ_{drift} and P_{drift} represent the total drift. This corresponds to values up to 10°and 5% in power for 2019/2020 and 3°and 2.5% for

2020/2021.
The total error of the calibrated data that is used for density reconstruction is the addition of the errors mentioned above, meaning $\delta\varphi_{\text{final}} = \delta\varphi_{\text{noise}} + \delta\varphi_{\text{drift}}(t)$ and $\delta P_{\text{final}} = \delta P_{\text{noise}} + \delta P_{\text{drift}}(t)$.
Some other sources of errors, like microwave radiation from plasma, were also analyzed but were found to be negligible [12].

An additional error that is not taken into account yet is introduced by the ELM removal algorithm itself. If the data used for the density reconstruction is averaged over a time period, an additional error should be taken into account, which depends on the level of the signal oscillation in this time window. A characteristic value for the signal oscillations (RMS, for example, if applicable) should be evaluated. This error needs to be added to the total error described above, both for the average density reconstruction and for the comparison of the experimental data to the modeling database, presented in the next section.

2.4 Comparison of experimental data to the synthetic diagnostic database

The processed calibrated data can be used for the density reconstruction. However, first an analysis of this data is done. It needs to be checked whether the experimental points lie inside the area covered by the modeled points, since the density can only be reconstructed from values, which lie within the database limits. Due to the complex shape of the modeling database, using a single area in MATLAB was not feasible and several areas were used, which together cover the whole database (shown for MILS 1.1 in Figure 25). Points outside the total area with an additional buffer layer are counted as points out of range. The buffer represents the errors in the modeling data and is applied as circles of a constant value at the edge points. This can be improved, as the buffer value of 0.2 corresponds to a power error of 20% and a phase error of 0.2°, which does not represent the actual errors. When looking for experimental points out of the described areas, the phase and power were averaged over 50 ms to exclude oscillations. Ideally an error bar for each experimental point has to be calculated to do a more precise analysis. In this case, a simplified analysis about the origin of points out of range in relationship to different plasma parameters is done and presented in the following.

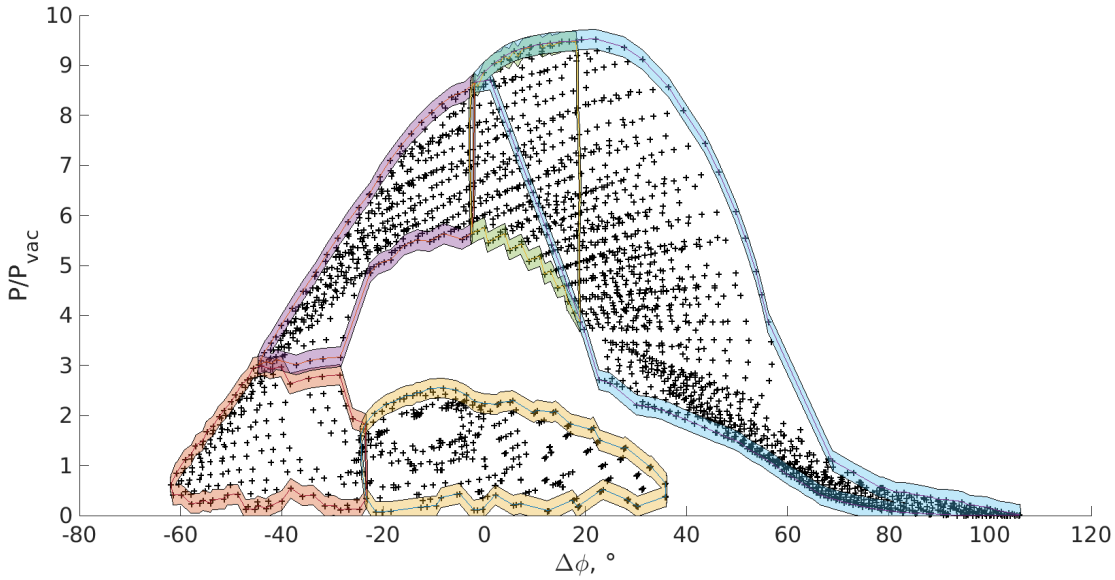

Figure 25: Different areas with a buffer created to cover all modeled points as accurate as possible. Points outside of all those areas including the buffers are counted as points out of range.

Different parameters of the discharges were checked for possible correlation with points out of range. These parameters are

- Density distribution shape deviation from the shape assumed in the modeling database caused by
  - Misalignment of the flux surfaces with the limiter contour
  - Poloidal density inhomogeneity caused by ICRH
  - Poloidal density inhomogeneity caused by resonant magnetic perturbations (RMPs)
- Phase and power drift due to thermal expansion (subsection 2.2.1)
- Low power values.

To find possible correlations between the parameters above and the points out of range in the phase power diagram, around 70 discharges were processed. The analysis showed a wide range of variety regarding the amount and time trace of points out of range. In some discharges not a single averaged point deviates from the modeled database. In other discharges however, the percentage of outliers ranges up to 80%. The distribution of the outlier points in time also differ significantly,

from being continuous after a certain point in time to being distributed over the whole stable plasma plateau.

In some cases, the calculation of the mean value over a 50 ms does not represent the actual background value for this interval. This can either origin from too many big oscillations or from removing too much data by the ELM removal algorithm. Only the data, for which the averaged signal provides meaningful value of the background density level, are considered in this analysis.

2.4.1 Deviation of the density distribution shape

As the modeling was done assuming radial plasma density decay and constant poloidal density, misalignment of flux surfaces in the MILS measurement region can introduce points out of the modeling database. This can either happen because of the choice of the plasma shape for a discharge, because of the application of the ICRH or when time varying 3D modification of the shape by RMP coils is done.

To check for possible misalignment of the flux surfaces in the MILS measurement region, values of the upper and lower plasma triangularity were checked. Triangularity is given by

$$\delta_{\text{upper}} = \frac{R_{\text{geo}} - R_{\text{upper}}}{a}, \delta_{\text{lower}} = \frac{R_{\text{geo}} - R_{\text{lower}}}{a} \tag{2.2}$$

with a being the minor radius, R_{geo} the geometric major radius, R_{upper} the major radius of the highest vertical point and R_{lower} the major radius of the lowest vertical point [19]. No obvious dependency between the points out of range and the triangularity was found when looking at the time evolution of the triangularity. To have a more precise criterion regarding the alignment of flux surfaces, two points within the MILS measurement region were chosen and the normalized plasma radius was calculated at those points. If the alignment is good, the difference between the plasma radii would be zero. The diagnostic chosen for the calculation of the flux surfaces is 'EQH', which is based on solving the Grad-Shafranov equation for the poloidal flux [20] [21]. The precision of the calculated normalized radius values depends on the precision of the equilibrium reconstruction in 'EQH'. Other equilibrium reconstruction methods can be used for a comparison. How the R and Z coordinates were chosen is explained in the following. The blue lines in Figure 26 indicate lines regarding the half power beamwidth, where the power of the radiation pattern drops to half of the one along the axis. Thus, the power outside the lines is negligible and the alignment of the flux surfaces is important only in the poloidal range between the calculated points. In the radial direction,

the limiter position is chosen for this evaluation, since it is the middle point of the radial range of the MILS measurements.

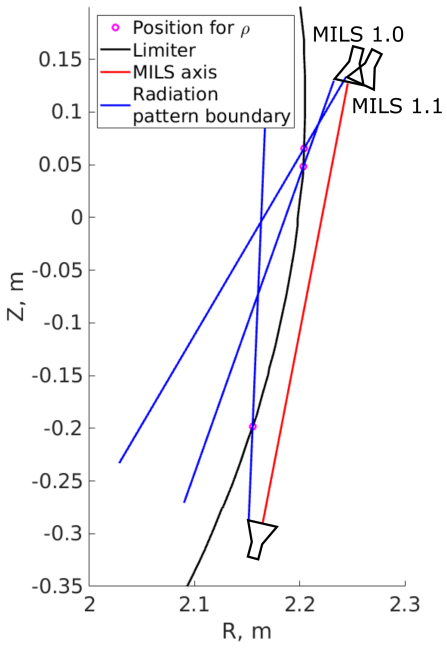

Figure 26: A sketch for the evaluation of the position of the normalized plasma radius at the limiter for the two different MILS configurations, with the MILS 1.0 axis shown in red.

The intersection points were calculated by intersecting the limiter (black) with those lines (blue). The resulting points are marked in magenta. The figure shows the two different MILS configurations, which led to different coordinates for the upper point. In red the MILS axis for MILS 1.0 is shown. For both configurations the coordinates for the lower point are $R_{\text{lower}} = 2.155\,\text{m}$ and $Z_{\text{lower}} = -0.198\,\text{m}$. For MILS 1.0 the coordinates of the upper point are given by $R_{\text{upper0}} = 2.203\,\text{m}$ and $Z_{\text{upper0}} = 0.048\,\text{m}$ and MILS 1.1 being $R_{\text{upper1}} = 2.204\,\text{m}$ and $Z_{\text{upper1}} = 0.065\,\text{m}$.

The analysis showed that the difference in the upper and lower value of the normalized plasma radius was always in the range of $-0.04 \leq \rho_{\text{upper}} - \rho_{\text{lower}} \leq 0.03$ but no obvious connection between the values or ranges for different percentages of points out of range could be found.
Poloidal density inhomogeneity can be present in the vicinity of active ICRH antennas. It is possible to disturb the density in the limiter region by the electric fields produced by the ICRH antenna. However, with the 3-strap ICRH antennas

at AUG it is possible to reduce the electric field at the antenna limiter position [22]. It is done through dipole phasing, meaning the current in the neighbor straps are in opposite direction. This configuration, where the electric field is most suppressed is called 'optimized configuration'. With this configuration, the ICRH would not have a strong effect on perturbing the density near the limiters and therefore would not introduce points out of range in the MILS phase power diagram. Thus, it is expected that points out of range do not correspond to the ICRH power. This could be confirmed by the analysis, investigating ICRH power values up to 3.5 MW.

Another possible cause for misalignment is the use of RMP coils to mitigate ELMs in H-mode [23]. The toroidal periodicity of the plasma edge undergoes noticeable deformation of the separatrix, altering it by a few percent of the minor radius due to the influence of the applied fields created by the RMP coils. When checking for possible effects on our signals, values above 500 A in the coils were taken into consideration, as a criterion that the coils were switched on. However, no obvious correlation between the current in the coils and points out of range in the phase power diagram could be found.

Summarizing the investigated points it can be said that the misalignment of the flux surfaces in the MILS measurement region or poloidal density inhomogeneity caused by ICRH or by RMPs are not strong enough to introduce discrepancies between the experiment and the model, where perfectly aligned shape and poloidally constant density are assumed. Another reason for the points not appearing as points out of range could be a shift in the phase power diagram, while staying inside the modeled database.

2.4.2 Phase and power drift

The magnitude of the total phase and power drift was also taken into account. It is expected that large drifts cause points to deviate from the model database. This can be explained by the compensation of the drift during the processing of calibrated data (section 2.2). A larger drift introduces a bigger error during the processing, which can lead to deviations from the modeled database. A general correlation between points out of range and the drift could not be found. It showed in many cases that phase drifts $|\varphi_{\text{drift}}| > 50°$or relative power drifts $|P_{\text{drift}}| > 0.09$ cause outliers. In some cases however, large drifts did not effect the points out of range at all. This needs further investigation.

2.4.3 Low power values

Finally, it was noticed that power ratio values < 0.05 lead to the phase value being scattered in a very wide range of values and therefore being located outside of the database boundaries. Low level of the power of the signal reaching the receiver in the high-density plasma leads to two reasons of increased errors in the data. First, low signal-to-noise ratio can lead to large errors or even to unusable data. Second, additional error in the phase detection is introduced, when the power level in the plasma path differs significantly from the power level in the vacuum reference path [12].

2.4.4 Remaining reasons

Furthermore, there are also other possibilities on why the experimental data does not correspond to the modeled one. As mentioned before, assumptions about the density profile of the plasma were made during the modeling process. Therefore possible errors could come from the differences in the density distribution shape between experiment and theory. Since the poloidal homogeneity and the alignment of flux surfaces were already discussed, the radial plasma density that was modeled by an exponential function and the perfect alignment of the MILS axis perpendicular to the background magnetic field are left to introduce discrepancies. However, since most of the experimental data lies within the boundaries determined by theory one can conclude that the assumptions made were suitable to represent the shape of the experimental density profile in most of the cases and only a insignificant part of the wave travels in X-mode.
Finally, there is the possibility that radiation from other diagnostics or other sources in plasma can cause points to deviate from the modeled database. However, it was observed that the diagnostics in AUG do not interfere with the MILS signals as they operate in different frequency ranges [12].

Keeping the mentioned aspects in mind, density reconstruction with the now calibrated data, according to subsection 1.3.3, can be done. The density reconstruction itself is not part of this thesis.

3 Discussion and Summary

The newly developed diagnostic MILS measures the density at the edge of the plasma in AUG. In order to reconstruct the background density profile a reliable processing algorithm for the MILS data is needed.

This algorithm called ELM removal algorithm was developed within this work. It works by taking the raw MILS signals, removing perturbations initially found by the "ELM" signal, improving the cutout done with the "ELM" signal and cutting high oscillations. The algorithm works well for many discharges, but not for all. In discharges with many small ELMs during a short period of time the algorithm removes too much data, which can be improved by making the removal of the ELMs dependent on the ELM duration and frequency. It was also noticed that not for every discharge the "ELM" shotfile is available. Therefore, only strong oscillations were cut by a part of the whole algorithm. One idea of improving this cases could be the application second part of the ELM removal algorithm after the oscillations are cut. During the calibration of the measured values to actual phase and power values, an analysis of the phase values was done. In the analysis of the raw phase signals, a dependency of the signals to the ICRH power was found. This can be explained by the phasing of the ICRH antennas.

The calibrated data is further processed by correcting the drift of the signals caused by thermal expansion. After the processing the experimental data is compared to the data obtained from full-wave 3D modeling. Different reasons for points being out of the modeled database are investigated. In general, it is possible that the mean value of the signals over 50 ms does not represent the actual background value of the signal, because too much signal is removed in certain intervals, which would introduce points deviating from the model. Apart from this reason, physical errors are analyzed. First, reasons for the density distribution shape to deviate from the shape assumed in the model were investigated. It became clear that poloidal density inhomogeneity introduced by ICRH or RMPs are not strong enough to introduce points out of range. Second, it is expected that large signal drifts due to thermal expansion of the MILS in-vessel components cause points to deviate. In many cases, correlation between the large drift values and the outliers was found, but in some cases with large drifts no outliers are observed. Further study of this correlation is needed. Third, low power values would correspond to the loss of the

microwave signal and therefore leads to points out of range caused by large phase errors. For the remaining discrepancies, a few assumptions can be made. For the modeling process, simplifications like the MILS axis being perfectly perpendicular to the background magnetic field decay were assumed. This might not depict reality as good as possible, as part of the wave could travel in X-mode, when the alignment is not perfect.

As a result of this work, improvements have been introduced to various aspects of the MILS data processing and some aspects which require further investigation have been identified.

Bibliography

1. Ritchie, H., Roser, M. & Rosado, P. Energy. *Our World in Data.* https://ourworldindata.org/energy (2022).
2. Ongena, J. & Oost, G. V. Energy for future centuries: Prospects for fusion power as a future energy source. *Fusion Sci. Technol.* **61,** 3–16 (2012).
3. Chen, F. F. *et al. Introduction to plasma physics and controlled fusion* (Springer, 1984).
4. Wesson, J. & Campbell, D. J. *Tokamaks* (Oxford university press, 2011).
5. Willensdorfer, M. Temporal behavior of the plasma edge density throughout the LH transition in ASDEX Upgrade (2013).
6. IPP. *Introduction: The ASDEX Upgrade tokamak* `https://www.ipp.mpg.de/16208/einfuehrung`. accessed Juli 3rd, 2023.
7. Willensdorfer, M. *et al.* Characterization of the Li-BES at ASDEX Upgrade. *Plasma Phys. Control. Fusion* **56,** 025008 (2014).
8. Griener, M. *et al.* Qualification and implementation of line ratio spectroscopy on helium as plasma edge diagnostic at ASDEX Upgrade. *Plasma Phys. Control. Fusion* **60,** 025008 (2017).
9. Grenfell, G. *et al.* High-heat flux ball-pen probe head in ASDEX-Upgrade. *Rev. Sci. Instrum.* **93** (2022).
10. Usoltceva, M., Heuraux, S., Khabibullin, I. & Faugel, H. A new technique for tokamak edge density measurement based on microwave interferometer. *Rev. Sci. Instrum.* **93** (2022).
11. Usoltceva, M. *et al.* Sensitivity of Microwave Interferometer in the Limiter Shadow to filaments in ASDEX upgrade. *Contrib. Plasma Phys.* **62,** e202100194 (2022).
12. Usoltseva, M. *et al.* Experimental validation of the intensity refractometry principle for density measurements at the edge of a tokamak. *Fusion Eng. Des.* **192,** 113783 (2023).
13. COMSOL. *COMSOL website* `https://www.comsol.com/`. accessed September 4th, 2023.

14. Stix, T. H. *Waves in plasmas* (Springer Science & Business Media, 1992).

15. Stangeby, P. C. *et al. The plasma boundary of magnetic fusion devices* (Institute of Physics Pub. Philadelphia, Pennsylvania, 2000).

16. Claeskens, G., Hjort, N. L., *et al. Model selection and model averaging* (Cambridge University Press Cambridge, 2008).

17. Scholkmann, F., Boss, J. & Wolf, M. An efficient algorithm for automatic peak detection in noisy periodic and quasi-periodic signals. *Algorithms* **5,** 588–603 (2012).

18. Wendler, D. Two-dimensional reconstruction of filament temperatures and densities with the thermal helium beam at ASDEX Upgrade. *Phys. Plasmas* (2023). Submitted.

19. Harrer, G. F. *On the origin and transport of small ELMs* PhD thesis (Wien, 2020).

20. McCarthy, P. J., Martin, P. & Schneider, W. The CLISTE interpretive equilibrium code (1999).

21. Schneider, W. *et al.* ASDEX Upgrade MHD equilibria reconstruction on distributed workstations. *Fusion Engineering and Design* **48,** 127–134 (2000).

22. Bobkov, V. *et al.* Progress in reducing ICRF-specific impurity release in ASDEX upgrade and JET. *Nuclear Materials and Energy* **12,** 1194–1198 (2017).

23. Kirk, A. *et al.* Understanding the effect resonant magnetic perturbations have on ELMs. *Plasma Physics and Controlled Fusion* **55,** 124003 (2013).

List of Figures